

WAGENINGEN UNIVERSITY AND RESEARCH

METEOROLOGY AND AIR QUALITY

MSC THESIS

The influence of snow patch size on local-scale
advection of sensible heat towards a patchy snow
cover

Author

Luuk VAN DER VALK

Supervisors

Chiel VAN HEERWAARDEN

Robin STOFFER

October 18, 2019

Abstract

Snowmelt is poorly modelled by climate and weather models, especially when the snow cover becomes patchy. This causes problems, for instance, for hydropower stations. One of the uncertainties in modelling snowmelt of a patchy snow cover, is caused by the local-scale advection of heat, which transports sensible and latent heat originating from bare ground towards the snow patches. Regarding this process, the role of patch size for snowmelt has shown some contradicting results by previous studies. Therefore, this study aims to provide insight in the role of snow patch size during snowmelt by performing direct numerical simulations. This enables us to study a turbulent flow above a constant patchy snow cover in detail. However, due to the computational constraints of direct numerical simulations, realistic cases will need to be simplified. In this study, the measurements performed on a single snow patch by Harder et al. (2017) are simplified and used as starting point for investigating the fluid dynamical influence of snow patch size on snowmelt due to local-scale advection of sensible heat. It was found that for a doubling and quadrupling of the average snow patch size with an unchanged snow cover fraction, the total snowmelt reduced with respectively 15% and 25%. The length of the snow patches was the main cause of this reduction, since the sensible heat fluxes at the leading edge of the snow patches are similar for each snow patch. Also, the decay of the sensible heat flux downstream from the leading edge is found to be independent of patch size. Therefore, at the downwind edge of longer snow patches, the sensible heat flux is lower, reducing the total snowmelt when snow cover fraction is constant. Furthermore, stability was only found to have an indirect effect through the wind field on the sensible heat fluxes. This stability effect was, next to the general behaviour of the system, captured by the model we developed and consists of just a few equations. This simple model describes the behaviour of the height of the internal boundary layer and sensible heat flux as a function of distance from the leading edge. Overall, this study has provided a first step towards a more thorough understanding on the role of snow patch size on snowmelt due to local-scale advection, which can be used in future modelling studies.

Acknowledgements

First of all, I would like to thank Chiel and Robin for supervising me during this thesis. I always enjoyed our meetings (except on that one occasion :p) and learned a lot from you. Also, I would like to thank all the students and teachers that participated in the thesis ring, as you helped me with all the useful feedback. Lastly, I would like to thank the various coffee groups for the fun intermezzos from the thesis with a special reference to the guys from the nice salad.

Contents

1	Introduction	1
2	Methods	5
2.1	System description	5
2.2	Dimensional analysis	6
2.2.1	Parameter derivation	6
2.2.2	Parameter estimation	7
2.2.3	Rescaling the model results to reality	9
2.3	Model description and set-up	12
2.3.1	Surface generation	13
3	Results	15
3.1	System characteristics	15
3.1.1	Formation of an internal boundary layer	16
3.1.2	Local advection	19
3.2	Effects patch size on snowmelt	22
3.2.1	Total snowmelt	22
3.2.2	Surface fluxes for individual patches	23
3.2.3	Model development	24
3.3	Rescaling to atmospheric values	30
4	Discussion	33
5	Conclusion	37
	References	39

1 Introduction

Snowmelt-dominated rivers are crucial for the global water supplies as these supply water to more than one sixth of the world population (Barnett et al., 2005). Additionally, snow is a natural way to store water during the cold months and it is released during spring and summer, when the water demands are also higher (e.g. Viviroli et al., 2007; Berghuijs et al., 2014). However, this source of water supply during the ablation season, i.e. the season in which snow melts, is affected by global warming (Mankin et al., 2015).

During the ablation season, the prediction of snowmelt can be complicated, as the melt is caused by a combination of multiple processes. In general, the dominant melting terms for a snowpack are radiation and turbulence. Initially, snowmelt is dominated by radiation, whereas over the course of the ablation season, turbulence-driven snowmelt becomes responsible for up to approximately 50% of the total melt (e.g. Pohl et al., 2006; Mott et al., 2011). This increasing importance is caused by the transformation of a continuous snow cover towards a patchy cover, which also complicates snowmelt predictions even further. The patches and associated processes are poorly modelled by climate and weather models, and therefore also introduce uncertainty in simulated temperature and river discharge (Balsamo et al., 2009).

For a patchy snow cover, two small-scale surface layer processes influence the turbulent heat fluxes significantly (e.g. Schlögl et al., 2018). Firstly, local advection of turbulent heat from the bare ground towards the snow patch arises from horizontal surface gradients in temperature and moisture (e.g. Mott et al., 2013; Harder et al., 2017). Secondly, a stable internal boundary layer (IBL) can form over a snow patch, due to the large difference between the characteristics of the snow surface and the bare ground (Garratt, 1990; Mott et al., 2016). Relatively warm air is advected from the bare ground to above the snow patch forming a highly stable IBL. Subsequently, the atmospheric boundary layer can decouple from the surface and suppress the advected turbulent heat fluxes towards the snow patch. The balance between these processes is mainly determined by wind velocity and topography (Fujita et al., 2010). For high wind velocities, heat advection becomes the dominant term due to large mechanical turbulence, whereas for low wind velocities and a concave topography boundary layer decoupling becomes more important (Mott et al., 2016). During this study, these processes will come by with a focus on the sensible heat flux.

In recent years, field measurements were used in order to identify these regulating processes of total advection of sensible and latent heat towards snow patches (Granger et al., 2006; Harder et al., 2017; Mott et al., 2013, 2017). Also, the depth of the stable IBL was attempted to be quantified during these measurements. Granger et al. (2006) reported that the IBL heightens with the roughness of the bare ground and therefore transports more heat towards the snow patch, due to increased turbulence and reduced near-surface stability. In addition to these findings, Mott et al. (2013) showed wind velocity and topography also to significantly influence the development of the IBL. In idealised conditions (i.e. smooth bare ground surface, low wind speed and a concave patch), the IBL decreases to a height of 0.3 metres, allowing almost no heat to be transported towards the snow, due to the extreme stability near the surface (Mott et al., 2017). Harder et al. (2017) identified that moisture transport could also be a significant source of heat, as the latent heat term was measured to cause 33% of the snowmelt, whereas sensible heat was responsible for 31%. This, however, depended significantly on the presence of upwind water, such as ponds or wet soils.

To capture the local advection of heat and the formation of the IBL in models, these processes are often parametrized. Liston (1995) related the local advection towards a snow patch to the fetch distance, whereas

Granger et al. (2002) expanded this relation based on the condition that the depth of the formed IBL over the patch is known. As this depth often is not measured, Granger et al. (2002) and Essery et al. (2006) proposed an overall parametrization for the total heat advection for a single patch.

Furthermore, Marsh et al. (1999) presented a method to express the efficiency of local scale advection towards snow, using a simple boundary layer model. Using this model, Marsh et al. (1999) reported an increase in advected sensible heat for a 50% snow cover from 3.8 Wm^{-2} for a single snow patch of 400 m to 18.9 Wm^{-2} for a 50% snow cover with multiple patches of 20 m. The total heat flux of the bare ground remained approximately constant between two situations and the heat flux of the snow increased significantly, which resulted in a more efficient local advection.

Recently, Mott et al. (2015) and Schlögl et al. (2018) performed more complex simulations on a patchy snow cover. In a combined model with ARPS (Advanced Regional Prediction System) and Alpine3D, both papers used a surface model which parametrizes the surface fluxes from the Monin-Obukhov bulk formulation from Monin and Obukhov (1954) combined with the stability corrections of Deardorff (1972). The assumptions made for deriving the general Monin-Obukhov bulk formulations are, however, violated for patchy snow covers (Monin and Obukhov, 1954; Weismann, 1977). In these cases, the horizontal homogeneity and constant turbulent fluxes throughout the surface layer cannot be assumed. The latter violations are caused by the development of the stable IBL above the snow patches. To overcome this problem, the Monin-Obukhov bulk formulations can be combined with stability corrections derived by for instance Schlögl et al. (2017). This method, however, already showed large errors over continuous snow covers, let alone patchy snow covers (Schlögl et al., 2018).

Moreover, the results of Schlögl et al. (2018) contradict the results of Marsh et al. (1999), since Schlögl et al. (2018) report small sensitivity of sensible heat fluxes and snowmelt to changes in patch size with constant snow cover. However, the model applied by Schlögl et al. (2018) was unable to resolve the leading-edge effect caused by the heterogeneous surface pattern, while the surface also had a unrealistic regular pattern. Furthermore, the study performed by Marsh et al. (1999), based there work on a 2D Boundary Layer Model with a regular tiled surface pattern, which based the estimated surface fluxes on parametrized turbulence.

Motivated by the uncertainty introduced by these studies, this thesis researches the influence of patch size on surface fluxes for individual snow patches as well as larger landscapes with a patchy snow cover. To eliminate parametrization uncertainties and unrealistic surfaces present in the discussed studies, a new type of simulations are applied, Direct Numerical Simulations (DNS), which resolves all the spatial and temporal scales of turbulence (for a brief description see Section 2.3). This simulation type has already proven its value in the field of fluid dynamics (Moin and Mahesh, 1998) and is now also starting to get used in atmospheric sciences with Coleman et al. (1990) as one of the first. van Heerwaarden et al. (2014) also used direct numerical simulations and performed the simulations in MicroHH 2.0, which has as advantage the ability to resolve flows near a complex surface. As the model has relatively high computational costs, this thesis also aimed to develop a simple model, consisting of a few equations. This model can describe and help understanding the development of the IBL and the accompanied surface heat fluxes over snow patches.

The aim of this study is to expand the recent research existing on a single snow patch towards a patchy snow cover and quantify the response of snowmelt, due to sensible heat fluxes, to changing patch size using DNS. To do so, initially, we compare simulations in MicroHH with the measurements on a single snow patch of Harder

et al. (2017), as these measurements are done in close to idealized settings on a flat surface. Subsequently, several simulations in MicroHH with changing patch size are compared, such that we can study the influence of patch size on sensible heat fluxes. To achieve this, we address the following research question during this thesis:

What is the influence of changing patch size on snowmelt driven by sensible heat for a patchy snow cover on an idealized flat surface?

2 Methods

In this chapter, initially system at stake is presented and rescaled in respectively sections 2.1 and 2.2. Subsequently, the model and the set-up are introduced in section 2.3.

2.1 System description

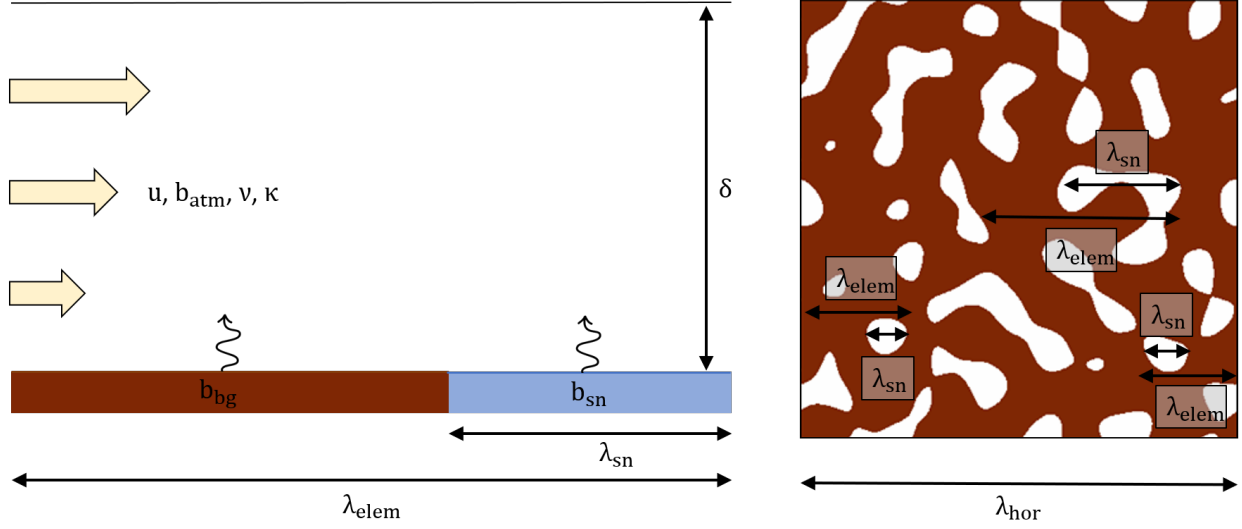


Figure 1 | Conceptual situation sketches. Sketches of one snow patch and the adjacent bare ground, i.e. an element, (left) and the horizontal domain with indicated element and snow patches (right).

The studied system consists of a near-neutral atmosphere above a patchy surface with heterogeneous properties and is based on the measurements on a single snow patch done by Harder et al. (2017) (Figure 1). This system can be described by the following variables:

$$(\nu, \kappa, u, \delta, \lambda_{hor}, \lambda_{elem}, \lambda_{sn}, b_{atm}, b_{sn}, b_{bg}). \quad (1)$$

The viscosity ν ($\text{m}^2 \text{s}^{-1}$), thermal diffusivity κ ($\text{m}^2 \text{s}^{-1}$) and wind speed u (m s^{-1}) describe the properties of the neutral atmosphere. δ (m) and λ_{hor} (m) respectively are the vertical and horizontal extent of the domain. λ_{elem} (m) represents the average size of one snow patch element, consisting of the snow patch itself (λ_{sn}) and the adjacent bare ground ($\lambda_{elem} \equiv \lambda_{bg} + \lambda_{sn}$). The buoyancy of the atmosphere (b_{atm}), the surface layer over the snow (b_{sn}) and the surface layer over the bare ground (b_{bg}) are defined as

$$b \equiv \frac{g}{\theta_{atm}}(\theta - \theta_{atm}), \quad (2)$$

in which g (m s^{-2}) is the gravitational acceleration and θ_{atm} (K) is the temperature of the atmosphere, which is assumed to be a constant during this study. This definition causes the temperature dimension to cancel out and m s^{-2} to remain as unit. In this study, we assume for each simulation that initially the simulated

atmosphere is well-mixed, such that the temperature of the atmosphere is constant over height (similar to Harder et al., 2017). This simplification results in b_{atm} to be zero.

Furthermore, we assume that the horizontal extent (λ_{hor}) is orders of magnitudes larger than the elements, such that λ_{hor} does not have an influence on the physics in the model. Thus, λ_{hor} is also not taken further into account in the following dimensional analysis.

To be able to identify the influence of snow patch size on snowmelt, λ_{sn} should obviously be varied with. The variations in snow patch size are done by doubling and quadrupling λ_{sn} compared to a reference simulation, which contains similar snow patches as Harder et al. (2017). Therefore, the latter simulation will be called Baserun. The simulations with a doubled and quadrupled snow patch size compared to the Baserun, will hereafter be called Patch 2 \times and Patch 4 \times . Furthermore, as our interest also lays with the role of stability on this system, an additional simulation is performed in which the system is the same as the Baserun, except that stability effects are excluded. In this simulation, the buoyancy behaves as a trace gas, such as methane, which does not influence the flow dynamics. This simulation will hereafter be referred to as Tracer simulation.

2.2 Dimensional analysis

2.2.1 Parameter derivation

In this study, the atmospheric turbulent channel flow from Moser et al. (1999) is taken as starting point for designing the experiments. To fit the measurements done by Harder et al. (2017) within the domain of this turbulent channel flow, a dimensional analysis according to Buckingham's Pi Theorem is used. This theorem allows to develop a minimal set of dimensionless parameters from the involved variables, which describes the system at stake. However, the exact influence of these variables on the system is unknown.

The system was originally described by ten variables, but is now reduced to eight variables, which all consist of two primary dimensions (i.e. length and time):

$$(\nu, \kappa, u, \delta, \lambda_{elem}, \lambda_{sn}, b_{sn}, b_{bg}). \quad (3)$$

All of these variables are nondimensionalized by using δ and u as repeating variables, since these cover both the primary dimensions, respectively [L] and [L T⁻¹], and are constant throughout all the numerical experiments. Thus, this results in six dimensionless groups, which can be combined into:

$$\left(\frac{\nu}{\kappa}, \frac{u\delta}{\nu}, \frac{\lambda_{sn}^2}{\lambda_{elem}^2}, \frac{\delta}{\lambda_{elem}}, -\frac{b_{sn}\delta}{u^2}, -\frac{b_{bg}\delta}{u^2} \right). \quad (4)$$

The nondimensional parameters can be interpreted as follows:

$\frac{\nu}{\kappa}$ is the Prandtl number (Pr). This is assumed to be constant throughout this study, such that the flow over the patchy surface always has the same characteristics and does not influence the outcome of the simulations. In this study, the number is set to one, instead of 0.71, which is the atmospheric value. This deviation has negligible impacts on the flow and allows for simpler scaling, when analyzing the simulations (Kawamura et al., 1998).

$\frac{u\delta}{\nu}$ is the Reynolds number (Re). For the same reason as the Prandtl number, this parameter is taken constant throughout the study. During this study, the same Reynolds number as Moser et al. (1999) is taken, being $1.10 \cdot 10^4$. This infers a wind speed of 0.11 m s^{-1} , a 1 meter vertical extent and a viscosity of $1.0 \cdot 10^{-5} \text{ m}^2 \text{ s}^{-1}$.

$\frac{\lambda_{sn}^2}{\lambda_{elem}^2}$ is the snow cover area fraction (SCF) and varies between zero and one. If this parameter is one, the field is completely snow covered, whereas values close to zero represent low snow covers. For all simulations, this dimensionless group is set to a value of 0.25 similar to Schlögl et al. (2018), as Harder et al. (2017) does not provide any information about this. This implies that 25% of each generated element is set as snow surface.

$\frac{\delta}{\lambda_{elem}}$ is a measure for the size of a surface element compared to the height of the system. This nondimensional number will decrease, if the typical element size increases. If the SCF is kept constant, changes in this variable will also affect the typical snow patch size, such that this variable becomes a measure for the relative snow patch size. Therefore, this dimensionless group will be varied throughout the simulations.

$-\frac{b_{sn}\delta}{u^2}$ is the bulk Richardson number above the snow patches (Ri_{sn}). Positive and negative values indicate respectively stability and instability, whereas large absolute values specify the magnitude of the (in)stability.

$-\frac{b_{bg}\delta}{u^2}$ is the bulk Richardson number above the bare ground (Ri_{bg}). For Ri_{bg} the same principles hold as for Ri_{sn} .

From the above mentioned dimensionless parameters, the former three are based on Moser et al. (1999) and Harder et al. (2017). The latter three will be calculated in the following section.

To research the influence of the patch size on snowmelt, the $\frac{\delta}{\lambda_{elem}}$ is studied by changing the value of λ_{elem} . Although this nondimensional parameter does not contain a unique variable, variations in λ_{elem} will only affect this parameter, as $\frac{\lambda_{sn}^2}{\lambda_{elem}^2}$ is kept constant. Variations in other variables, such as δ , affect more than one of the six nondimensional parameters and are therefore less suitable as a changing variable throughout this study.

2.2.2 Parameter estimation

As mentioned in the previous section, the settings of the in-MicroHH-validated case for turbulent channel flow from Moser et al. (1999) are used as starting point for designing the experiments. These settings are combined with the measurements done by Harder et al. (2017) through the dimensionless parameters, such that the numerical experiments behave similar to the measurements.

To do so, first the values of the defined dimensionless parameters are calculated by using the measurements of Harder et al. (2017) (Table 1). Note that not all variables used in the dimensionless parameters are known, and are therefore estimated based on other literature, such as Schlögl et al. (2018) (Table 2). Subsequently, the variables coming from Moser et al. (1999) are filled into the nondimensional parameters, such that the remaining variables can be calculated.

Table 1 | Dimensionless parameter values. Overview of the applied values for the dimensionless parameters during the simulations.

	Pr	Re	SCF	δ/λ_{elem}	Ri_{sn}	Ri_{bg}
Baserun	1.00	$1.10 \cdot 10^4$	0.25	3.33	0.66	0.00
Tracer simulation	1.00	$1.10 \cdot 10^4$	0.25	3.33	0.66 ¹	0.00 ¹
Patch 2×	1.00	$1.10 \cdot 10^4$	0.25	1.67	0.66	0.00
Patch 4×	1.00	$1.10 \cdot 10^4$	0.25	0.83	0.66	0.00

Table 2 | Variable values applied in the simulations. Overview of the values used for obtaining the dimensionless parameters in the simulations. * are values that are estimated based on Schlögl et al. (2018).

Variables	Harder et al. (2017)	Moser et al. (1999)	Simulations
$\nu (m^2 s^{-1})$	-	$1.0 \cdot 10^{-5}$	$1.0 \cdot 10^{-5}$
$\kappa (m^2 s^{-1})$	-	$1.0 \cdot 10^{-5}$	$1.0 \cdot 10^{-5}$
$u (m s^{-1})$	6.4	0.11	0.11
$\delta (m)$	100*	1.00	1.00
$\lambda_{elem} (m)$	30*	-	0.30, 0.60, 1.20
$\lambda_{sn} (m)$	15	-	0.15, 0.30, 0.60
$b_{sn} (m s^{-2})$	-0.28	-	$-8.0 \cdot 10^{-3}$
$b_{bg} (m s^{-2})$	0.0	-	0.0

For example, the calculation of the buoyancy above snow needed in the simulations is done by using the Richardson number for snow. This Richardson number arises from:

$$Ri_{sn} \equiv -\frac{b_{sn,meas}\delta_{meas}}{u_{meas}^2} = -\frac{-0.28 \text{ m s}^{-2} \cdot 100 \text{ m}}{6.40^2 \text{ m}^2 \text{ s}^{-2}} = 0.66 \Rightarrow -\frac{b_{sn,sim}\delta_{sim}}{u_{sim}^2} = 0.66. \quad (5)$$

Subsequently, the characteristics of the system need to be implemented into the simulations and thus have the same value in these simulations. From Moser's case, it follows:

$$u_{sim} = 0.11 \text{ m s}^{-1}, \quad (6)$$

while δ in the simulations is already determined by Moser et al. (1999), as the height of the system is 2 m, and δ half the height of the system. Therefore the simulated buoyancy over the snow is,

$$Ri_{sn} = 0.66 = -\frac{b_{sn,sim}\delta_{sim}}{u_{sim}^2} \Rightarrow b_{sn,sim} = -\frac{0.66 \cdot 0.11^2 \text{ m}^2 \text{ s}^{-2}}{1.0 \text{ m}} = -8 \times 10^{-3} \text{ m s}^{-2}. \quad (7)$$

¹These are in fact not real Richardson numbers as buoyancy does not affect the flow in the Tracer simulation.

2.2.3 Rescaling the model results to reality

After nondimensionalizing and downscaling the system for the simulations, the outcomes of the simulations are rescaled back to realistic scales. For intercomparisons between simulations no rescaling is needed, as the modelled variables are multiplied with a factor to return to atmospheric values, which is constant throughout all simulations. This causes the absolute differences between simulations to change, but the relative outcomes of the simulations remain the same. However, to be able to state something about individual simulations and say something about how the simulations relate to reality, the results will need to be rescaled back to reality. In order to do so, the non-dimensional numbers need to be taken into account, as these numbers state something about the dominant processes within the system.

Surface heat fluxes rescaling

For rescaling the surface heat fluxes back to reality, the Ri_{sn} affects the rescaling factor being used. The number describes whether shear-driven turbulence or buoyancy-driven turbulence or a balance between the two is more dominant in the system, and thus also which process predominantly affects the surface buoyancy flux scaling. When analysing the results, the simulated Ri_{sn} will be calculated over the formed IBL instead of the atmospheric layer δ being considered, as this will describe the bulk Ri_{sn} near the surface, in which this study is interested. When shear-driven turbulence can be assumed to be dominant in the inner layer (i.e. near the surface), the equation becomes

$$B_0 = ub_{sn}, \quad (8)$$

in which B_0 is the typical buoyancy surface flux ($\text{m}^2 \text{s}^{-3}$), b_{sn} the surface buoyancy of snow (m s^{-2}) and u is the wind speed (m s^{-1}). This equation is derived from the original equation for the surface buoyancy flux implemented in the model

$$B_0 = -\kappa \frac{\partial b}{\partial z} \Big|_{sn}, \quad (9)$$

$$\sim \kappa \frac{b_{sn}}{\delta_v},$$

in which δ_v is the depth of the viscous sublayer (m), which is assumed to be in the order of magnitude of δz , whereas b_{sn} is assumed to be a measure for δb .

Equation 9 follows from a definition of the height of the viscous sublayer δ_v , for circumstances in which shear dominates, such that the δ_v is determined by wind and viscosity. This allows to set up a relation between these three variables

$$\delta_v = f(u, \nu), \quad (10)$$

$$\sim \frac{\nu}{u}.$$

When implementing this into Equation 9, to make Equation 8

$$B_0 \sim \kappa \frac{b_{sn}}{\left(\frac{\nu}{u}\right)} = \kappa u \frac{b_{sn}}{\nu} = u b_{sn}, \quad (11)$$

in which κ and ν cancel out, since Pr (i.e. $\frac{\nu}{\kappa}$) is unity in this study. Subsequently, this equation can be used to rescale the simulated surface buoyancy fluxes back to realistic values, according to

$$\frac{B_{0,sim}}{B_{0,real}} = \frac{u_{sim} b_{sn,sim}}{u_{real} b_{sn,real}}. \quad (12)$$

From Table 2 it follows that $b_{sn,sim} = -0.008 \text{ m s}^{-2}$, $b_{sn,real} = -0.28 \text{ m s}^{-2}$, $u_{sim} = 0.11 \text{ m s}^{-1}$ and $u_{real} = 6.4 \text{ m s}^{-2}$, thus the equation reduces to

$$\frac{B_{0,sim}}{B_{0,real}} = \frac{0.11 \times -0.008}{6.4 \times -0.28} = 4.9 \times 10^{-4}. \quad (13)$$

Thus, if it turns out that wind shear is the dominant process for the heat fluxes, the simulated values for the surface buoyancy fluxes are divided by 4.9×10^{-4} to compute the realistic values.

Another possibility is the dominance of buoyancy-driven turbulence, causing the equation for typical buoyancy scales to become

$$B_0 = b_{sn}^{4/3} \kappa^{1/3}, \quad (14)$$

in which κ is the thermal diffusivity ($\text{m}^2 \text{s}^{-1}$) (van Heerwaarden and Mellado, 2016). As the flow is assumed to be naturally convective (i.e. the only fluid motion is due to convection) and the height of the system is high enough, such that the surface fluxes are not affected by the height of the system, the only variables affecting the height of the viscous sublayer are b_{sn} and κ , which thus can be used to come up with a relation between the 3 variables

$$\begin{aligned} \delta_v &= f(b_{sn}, \kappa), \\ &\sim \left(\frac{\kappa^2}{b_{sn}}\right)^{1/3}. \end{aligned} \quad (15)$$

When implementing this into Equation 9, to make Equation 14

$$B_0 \sim \kappa \frac{b_{sn}}{\left(\frac{\kappa^2}{b_{sn}}\right)^{1/3}} = b_{sn}^{4/3} \kappa^{1/3}. \quad (16)$$

Again, this equation can be used to rescale the surface buoyancy flux back to reality, according to

$$\frac{B_{0,sim}}{B_{0,real}} = \frac{b_{sn,sim}^{4/3} \kappa^{1/3}}{b_{sn,real}^{4/3} \kappa^{1/3}}. \quad (17)$$

As shown in Table 2, $b_{sn,sim} = -0.008$ and $b_{sn,real} = -0.28$, thus Equation 17 reduces to

$$\frac{B_{0,sim}}{B_{0,real}} = \left(\frac{-0.008}{-0.28} \right)^{4/3} = 8.7 \times 10^{-3}. \quad (18)$$

As the ratio between the simulated and real buoyancy surface fluxes is now known, the values for the surface buoyancy fluxes from the simulations can be divided by 8.7×10^{-3} to come up with the realistic values.

The determination of the dominant cause for the behaviour of the surface buoyancy fluxes is done in the Results section. Subsequently, the outcome for the realistic surface heat fluxes can be transformed to W m^{-2} according to

$$H_{real} = \rho c_p \frac{\theta_0}{g} B_{real}, \quad (19)$$

in which H is the sensible heat flux (W m^{-2}), ρ the density of the air (kg m^{-3}), c_p the specific heat capacity ($\text{J kg}^{-1} \text{K}^{-1}$), θ_0 the reference temperature, being 273 K in this case and g the gravitational acceleration (m s^{-2}).

Time rescaling

For rescaling simulated time back to reality, the typical timescale is again considered to originate from a dimensional number, as these numbers describe the system being considered. Similar to the surface heat flux rescaling, the bulk Richardson number above snow ($Ri_{sn} = -\frac{b_{sn}\delta}{u^2}$) is again chosen, as the number determines the dominant turbulent process in the system (i.e. buoyancy versus shear). From the bulk Richardson number above snow, two intuitive timescales can be derived

$$\begin{aligned} \frac{\delta}{u} &= t_{adv}, \\ \left(\frac{\delta}{-b_{sn}} \right)^{\frac{1}{2}} &= t_{buoy}, \end{aligned} \quad (20)$$

in which T_{adv} resembles an advective timescale and T_{buoy} is a buoyant timescale. Just as the surface heat fluxes, we determine which defined timescale is used for scaling in the Results section. For now, both are elaborated upon. When calculating the ratios between the simulated and measured timescales by making use of the values in Table 2, the following ratios between the simulated and realistic timescales arises

$$\begin{aligned} \frac{t_{adv,sim}}{t_{adv,meas}} &= \frac{9.09}{15.63} = 0.58, \\ \frac{t_{buoy,sim}}{t_{buoy,meas}} &= \frac{11.18}{18.90} = 0.59. \end{aligned} \quad (21)$$

Thus, both ratios between the simulations and the realistic values are similar. However, for the sake of elegance in the Results section the correct timescale is determined.

2.3 Model description and set-up

In this study, the simulations are performed using the MicroHH 2.0 code, which is primarily made for DNS of atmospheric flows over complex surfaces by van Heerwaarden et al. (2017). The code of MicroHH has been written such that simulations can be conducted for three dimensional fluid dynamical problems accompanied with high Reynolds numbers. When solving the conservation equations for mass, momentum and energy, MicroHH makes use of the Boussinesq approximation. Moreover, MicroHH uses periodic boundary conditions in the horizontal directions, such that flow that goes out on one side of the system, comes in on the opposite side of the system with the same flow characteristics.

In general, DNS resolves all the turbulent scales in a flow from the largest eddies to the eddies which are affected by viscosity and are characterised by the Kolmogorov scale (Ferziger and Peric, 2002). As a consequence, the resolution should fulfill the condition of being able to solve the Kolmogorov scale, while the domain size should be large enough to capture the largest eddies. For the former condition, it also holds that the amount of grid points are proportional to the Reynolds number (Re) to the power $3/4$ (Tennekes and Lumley, 1972), and are a measure for the computational costs of the simulations. Furthermore, as Re^3 is approximately proportional to the costs of a simulation, Re is often kept relatively low, compared to real world Re . In such a case, it is assumed that this difference does not affect the outcome of the simulations.

The reduced Re also holds for this study, since the starting point for designing the numerical experiments is the atmospheric turbulent channel flow (Re_τ) designed by Moser et al. (1999). The shear Reynolds number Re_τ obtained from the measurements performed by Harder et al. (2017) is relatively high compared to Moser et al. (1999); $\sim 6 \cdot 10^6$ vs. 590, but the results of Moser et al. (1999) suggest that the bulk statistics, i.e. mean and variances, of the flow are hardly affected by this difference in Re_τ . This channel flow is simulated in MicroHH at a resolution of $384 \times 192 \times 128$ grid points, which is halved compared to Moser et al. (1999), for a domain size of $2\pi \text{ m} \times \pi \text{ m} \times 2 \text{ m}$. We assume that the resolution reduction does not affect the outcome of this study. The flow is forced in the x-direction by imposing an average wind speed, which is in this case 0.11 m s^{-1} . At the bottom and top boundary, no slip and no penetration conditions are applied to the velocities (i.e. the flow velocity at the boundary is zero). Furthermore, no buoyancy effects are included in this channel flow. Overall, van Heerwaarden et al. (2017) showed that MicroHH is well able to reproduce this turbulent channel flow.

Initially, the turbulent channel flow from Moser et al. (1999) is simulated until 1800 seconds, such that the turbulent channel flow has well developed. Subsequently for each simulation, this turbulent channel flow is adapted, such that an atmospheric flow over a patchy snow surface is obtained. On the bottom boundary, a pattern of surface buoyancies depending on the simulation is prescribed, such that the surface characteristics determined during the dimensional analysis are fulfilled. For snow and bare ground, the surface buoyancy is respectively $-8 \times 10^{-3} \text{ m s}^{-2}$ and 0.0 m s^{-2} . For the Baserun, on average snow patches of 0.15 m are implemented with an average element length of 0.30 m. For the Tracer simulation, the same snow patch distribution is implemented, as the only difference between the Tracer simulation and the Baserun, is the exclusion of stability effects in the Tracer simulation. For the Patch $2\times$, the snow patches are on average 0.30 m with an average element length scale of 0.60 m. Similarly for the Patch $4\times$, the average snow patches are 0.60 m and the average element length scale is 1.20 m.

2.3.1 Surface generation

To create the surfaces for the simulations, noise is generated in the Fourier space, such that seemingly random patterns with a specified wavelength arise. These wavelengths are prescribed in the form of 2D power spectra. This method is applied, such that the patches at the opposing walls fit together and flow that leaves the system on one side, continues over the same snow patch when it re-enters the system on the opposite wall. This enables the model to solve the periodic boundary conditions.

Initially, a field with random phases between 0 and 2π is generated. These phases are applied in Euler's law (i.e. $e^{i\varphi} = \cos \varphi + i \sin \varphi$), such that the phases are described in exponential form. The phases are multiplied with the desired magnitude per phase, such that the Fourier space is generated ($z = |z|e^{i\varphi}$ and Figures 2 - 4). Eventually, a 2D field with dominant patterns is obtained by returning to physical space by using the Inverse Fast Fourier Transform on the Fourier space. Also, to avoid numerical instabilities in MicroHH a Gaussian Filter is applied on the surface with a standard deviation of 1 grid cell. When this filter overlaps the edges of the domain, the values at the opposing edge are applied.

The specified spectra for all generated surfaces consist of two broad peaks (Figures 2 - 4). The peak with the lowest wavenumber has the higher factor and, thus, gives the dominant structures to the snow patch distribution. The peak with the higher wavenumbers (i.e. 3 times the average wavenumber of the main peak) has a lower factor, such that within the larger structures some smaller fluctuations occur, giving the patches a more realistic appearance. For the patch $2\times$ surface and $4\times$ surface, the wavenumber of the main peak has been reduced with a factor 2 and 4 respectively compared to the Baserun surface. This implies an average length of the snow patches in reality of 15 m, 30 m and 60 m for the Baserun, patch $2\times$ and patch $4\times$ simulations respectively.

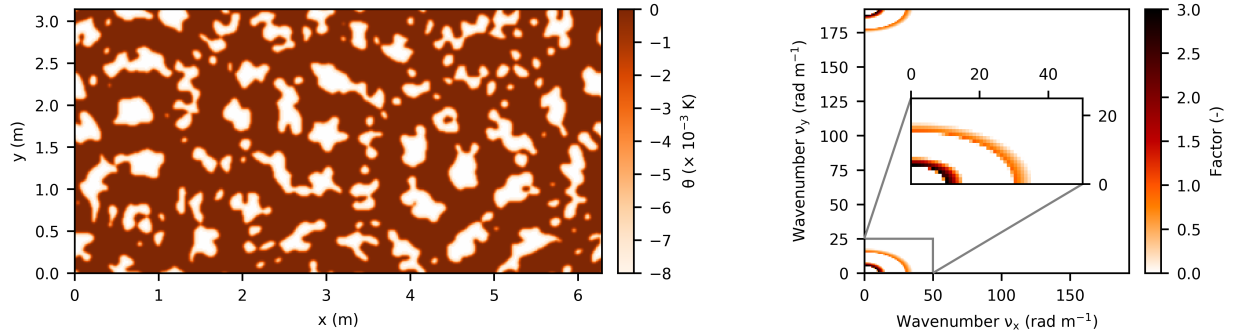


Figure 2 | Generated surface buoyancy acceleration and the applied Fourier space in absolute form for the Baserun and Tracer simulation. The generated surface buoyancy acceleration (left) obtained by applying the Inverse Fast Fourier Transform on the Fourier space (right).

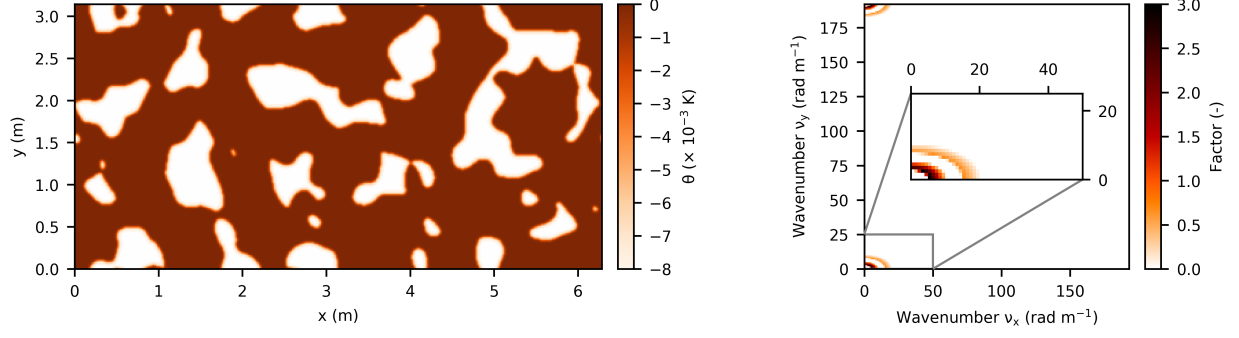


Figure 3 | Generated surface buoyancy acceleration and the applied Fourier space in absolute form for the Patch 2 \times simulation. The generated surface buoyancy acceleration (left) obtained by applying the Inverse Fast Fourier Transform on the Fourier space (right).

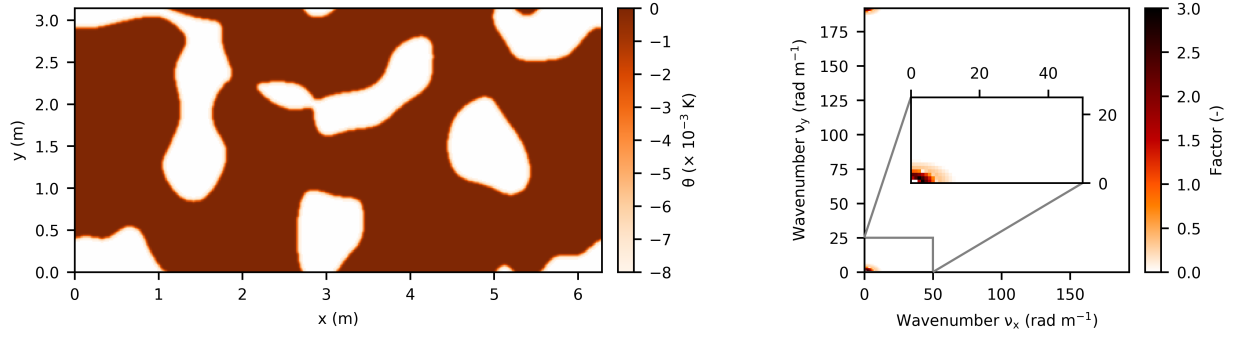


Figure 4 | Generated surface buoyancy acceleration and the applied Fourier space in absolute form for the Patch 4 \times simulation. The generated surface buoyancy acceleration (left) obtained by applying the Inverse Fast Fourier Transform on the Fourier space (right).

3 Results

This chapter starts with a mainly qualitative description of the system characteristics in the Baserun in section 3.1 to identify the dominant processes. In this first section, we aim to provide a more thorough understanding on the formation of the IBL and the wind pattern, which combined determine the local advection of sensible heat. Subsequently, based on this description, the differences between the Baserun (simulation with stability effects with similar patches as Harder et al. (2017)) and the other experiments are analysed in section 3.2, such that the influence of patch size on local-scale advection towards snow patches can be studied. Finally in Section 3.3, some of the graphs are rescaled back to realistic values to compare with previous studies.

3.1 System characteristics

The time averaged surface buoyancy fluxes resemble the implemented surface pattern of snow patches (Figure 5). There is a negative surface flux on the snow patches, whereas at the bare ground the surface flux is positive.

For each single snow patch, there is a clear pattern arising. The leading edge of the snow patches shows the highest buoyancy fluxes towards the surface (i.e. negative values) and decreases downwind of the leading edge until the end of the patch. Subsequently, at the trailing edge of the snow patch and leading edge of the bare ground, the buoyancy flux changes sign, as the bare ground is relatively warm compared to the colder air coming from above the snow patch. The air warms when flowing over the bare ground, such that when the air arrives at the next snow patch, it is relatively warm compared to the cold snow patch, causing a high downward flux.

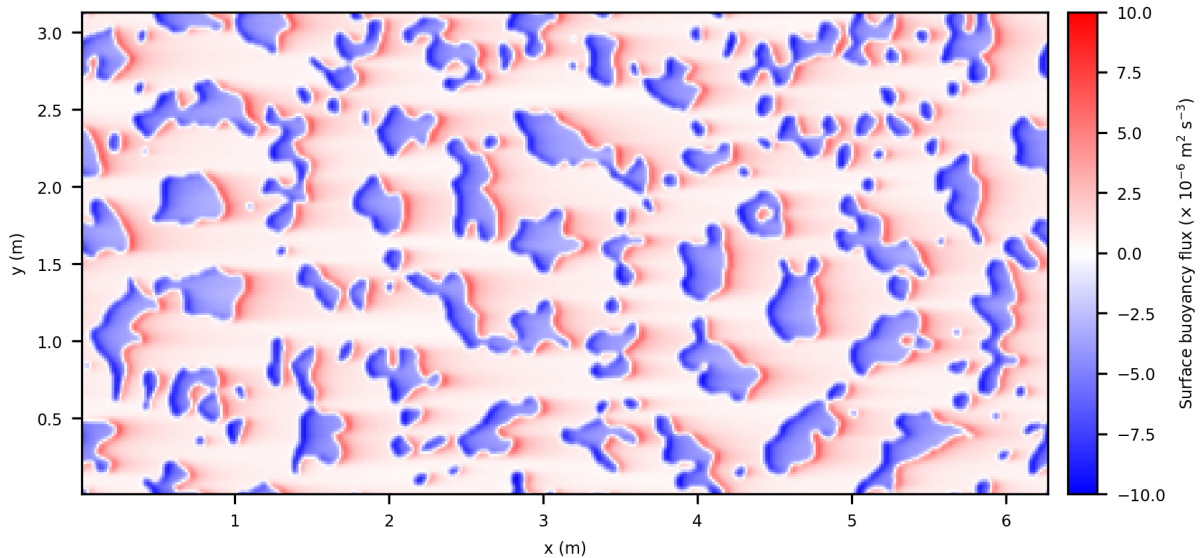


Figure 5 | Time averaged surface buoyancy fluxes. Surface buoyancy fluxes in the Baserun averaged from 2000 seconds until 2700 seconds. Negative values indicate a downward flux, whereas positive values resemble an upward flux.

3.1.1 Formation of an internal boundary layer

Vertical profiles of the buoyancy acceleration show clear IBL formation above snow patches as well as bare ground (Figure 6). For snow, a highly stable IBL forms above the surface, as the buoyancy at the surface increases with approximately 0.006 m s^{-2} (rescaled to reality approximately 6 K) in on average 0.025 m (rescaled to reality 2.5 m) (Figure 6). Also, at the leading edge of the snow patch, some remnant of warm air coming from the bare ground is present, although it is dissipated within approximately 0.03 m (rescaled to reality 3 m). For bare ground, however, the IBL formation is dominated by the remnant of cold air originating from the snow. The plume of cold air is dissipated throughout the course of the bare ground patch.

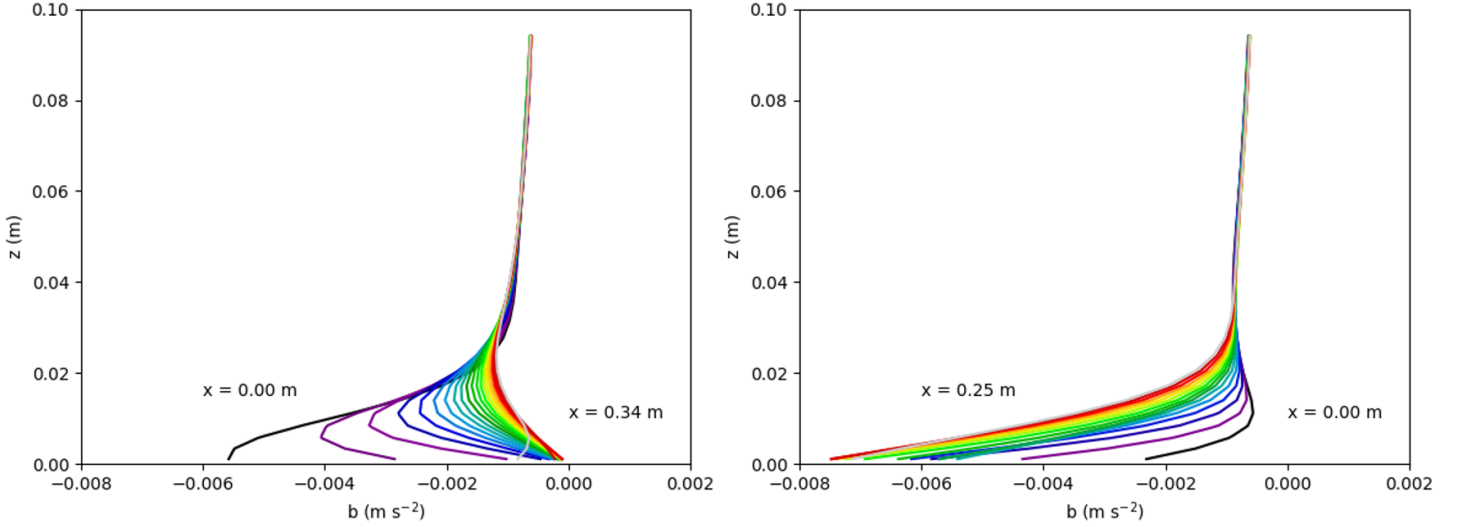


Figure 6 | Vertical buoyancy acceleration profiles at the bare ground patch at $y = 0.83 \text{ m}$ and $x = 3.75 \text{ m}$ (left) the snow patch at $y = 0.83 \text{ m}$ and $x = 3.95 \text{ m}$ (right) in the Baserun simulation. The labels with 'x =' show the location of vertical profile related to the downwind distance of the leading edge of the snow patch. The line colors represent distance from the leading edge and go from blue (leading edge) to red (downwind edge).

The vertical profiles do not coincide with the vertical profiles reported by Harder et al. (2017), on which the Baserun is based. The shape of the profiles over the snow patch are similar to Harder et al. (2017) as well as Mott et al. (2016), who performed measurements in a wind tunnel with different circumstances. The height, however, at which temperature becomes constant over height is approximately 5 times larger in our simulations compared to Harder et al. (2017); 2.5 meter for the model versus 0.5 m. This mismatch is probably caused by the relatively low Reynolds number used in the simulations. This low Reynolds number causes the buoyancy fluxes in the IBL to be dominated by diffusive fluxes (Figure 7), because the height of a diffusive layer scales with the $Re^{-3/4}$ (Tennekes and Lumley, 1972). In the IBL, the turbulent buoyancy fluxes are on average even upward, due to the strong downward diffusive flux.

For bare ground, the shape of the vertical profiles does not coincide with the profiles of Harder et al. (2017), in which the cold air plume is not found. However, when extrapolating the development of the bare ground profiles in Figure 6, the profiles become more alike as the cold air plume dissipates and results in an approximate constant temperature over height. This would imply that the bare ground patch on which measurements were performed by Harder et al. (2017) was relatively long.

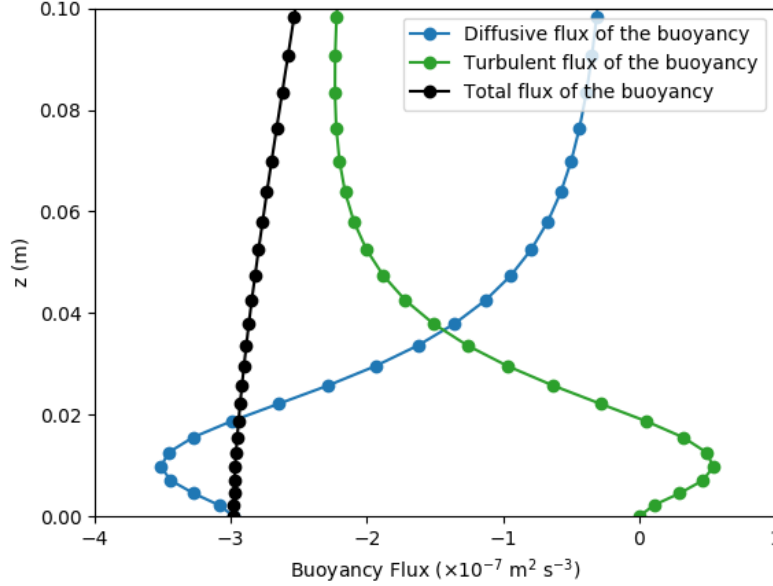


Figure 7 | Vertical profile of the diffusive, turbulent and total buoyancy flux. Vertical profile of the diffusive buoyancy, turbulent and total buoyancy flux in the Baserun averaged from 2000 seconds until 2700 seconds over the whole horizontal domain.

The influence of the IBL becomes evident from the differences in surface buoyancy flux between the Baserun, with stability effects, and the Tracer simulation, without stability effects. The surface buoyancy flux of the snow patches is less negative for the Baserun than the Tracer simulation (Figure 8). This suggests the presence of relatively cold air above the snow patches during the Baserun compared to the Tracer simulation, which is confirmed by the xz-cross section of the buoyancy (Figure 9).

The stable stratification above the snow patches causes the cold air to stick close to the surface (i.e. approximately the lowest 0.05 meter), whereas on higher altitude the air is warmer for the Baserun than the Tracer simulation (Figure 9). The cold air at the surface resembles the formed IBL, which enables the air above it to decouple from the surface, due to the stably stratified surface layer. This decoupling reduces mixing over height, causing the air above the IBL to be warmer for the Baserun compared to the Tracer simulation. Also, the decoupling causes a lower buoyancy gradient between the snow patches and the air above within the IBL, such that the heat flux towards the patch is relatively small.

Furthermore, downwind of every snow patch, the buoyancy close to the surface is slightly higher for the Baserun than the Tracer simulation (Figure 9). This indicates the formation of another IBL being located above the bare ground. This IBL is weaker compared to the IBL above the snow patches, as this IBL is unstable and the buoyancy of the bare ground is relatively close to the air buoyancy outside the IBL. However, the presence of the warm air over the bare ground causes a lower buoyancy gradient between the bare ground and the surface air for the Baserun, such that the buoyancy flux from the bare ground is less positive for the Baserun.

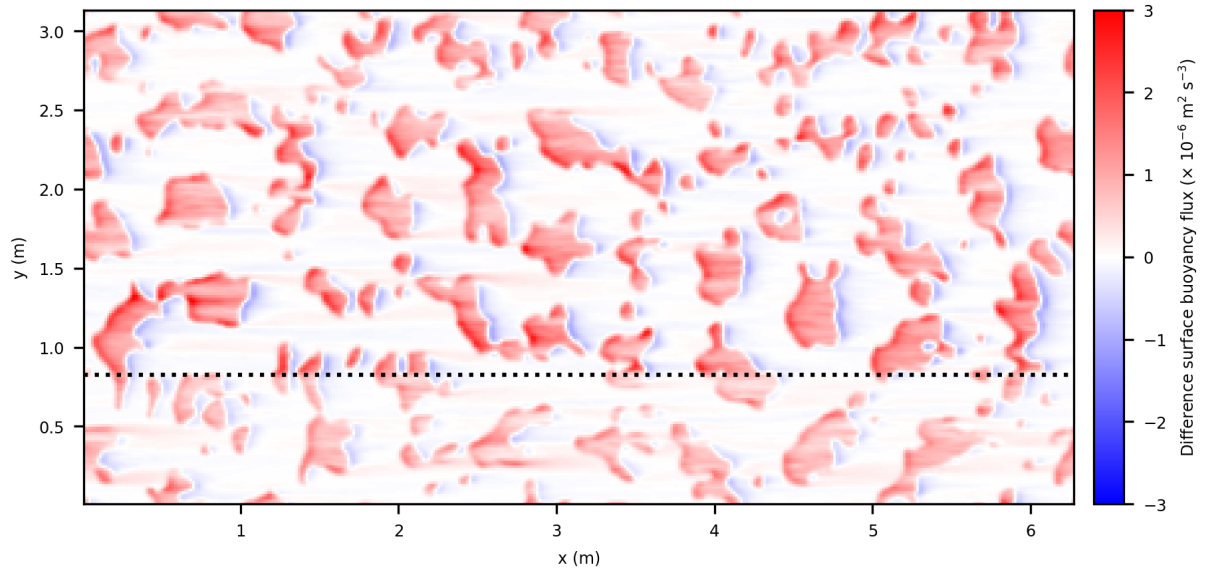


Figure 8 | Comparison between the Baserun and the Tracer simulation in time averaged surface buoyancy fluxes. Difference in surface buoyancy fluxes between the Baserun and the Tracer simulation (Baserun - Tracer simulation) averaged from 2000 seconds until 2700 seconds. The dotted line shows the location of the cross section in the xz-plane given in Figure 9.

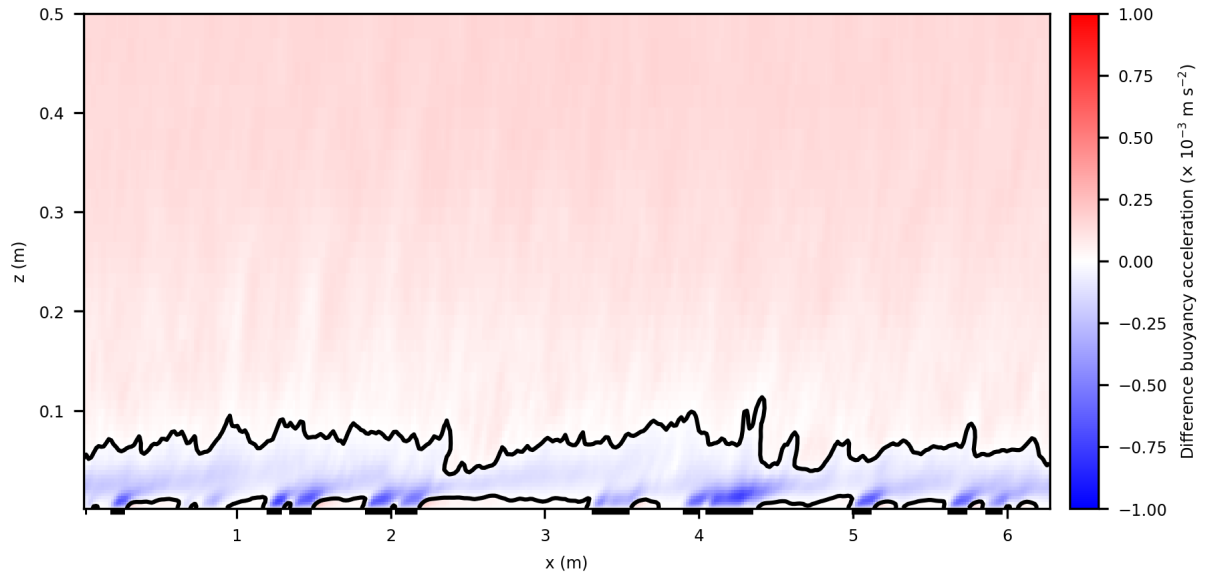


Figure 9 | Comparison between the Baserun and the Tracer simulation in the time averaged buoyancy acceleration in the xz-plane. Cross section of the difference in buoyancy acceleration between the Baserun and the Tracer simulation (Baserun - Tracer simulation) in the xz-plane at $y = 0.83$ m averaged from 2000 seconds until 2700 seconds. The thicker parts of the x-axis indicate the location of a snow patch. The contour line is the difference between negative and positive differences.

3.1.2 Local advection

The formation of the IBL, discussed in the previous section, also has an influence on the flow field. Close to the surface the wind speed in the x-direction is on average smaller for the Baserun compared to the Tracer simulation. However, the maximum wind speed is higher for the Baserun than the Tracer simulation (Figure 10), which supports the found decoupling based on Figure 9. Above the viscous sublayer (i.e. approximately 0.01 to 0.02 m), the wind profile of the Baserun seems to be logarithmic as the profile follows a reasonable straight line. For the Tracer simulation, being a turbulent channel flow with buoyancy behaving as a trace gas, the wind profile resembles less of a straight line. However, a logarithmic wind profile is one of the characteristics for turbulent channel flow. This could be caused by the relatively short time averaging, as turbulent channel flows can contain long-lasting turbulent structures affecting the wind profile. For the log-profile of the Tracer simulation, the gradient is higher and, thus, the friction velocity lower compared to the Baserun, showing the stability effects on the wind field.

At the lowest grid level, the influence of the patches on the wind becomes evident, as all the patches reduce the wind speed in the x-direction (Figure 11A). This bubble of air above the patches with a reduced momentum in the x-direction behaves as a barrier, such that the flow field is also affected in the y and z-direction (Figure 11B and C). At the leading edge, the air tends to move around the snow patches or, to a lesser extent, upwards and over the snow patches, whereas the latter mainly holds for some larger patches. This detour around and over snow patches possibly reduces the amount of sensible heat advected from the bare ground to reach the snow patches.

However, striking are the highest vertical wind speeds, which do not occur over the larger snow patches, but arise mainly at or close to the edges of the larger patches (Figure 11C). This location is caused by the convergence of the flow in the y-direction at the edges of the patches (e.g. at $x = 1$ m, $y = 1.5$ m). As the air is blocked by the surface, the air is forced upwards or downstream, due to which the relatively high wind velocities in a elongated pattern arise in the x and z-direction (Figure 11A and C). Also, the enhanced vertical wind speeds at the edges of the patches seem to induce a downward movement above the patches, although these are of a smaller order of magnitude than the upward movement. Thus, a circulation in the yz-plane arises, due to the flow influences of the snow patches. This circulation advects relatively cold air originating from the patches away from the surface towards a higher altitude. Meanwhile, the downward movement advects relatively warm air from higher altitudes towards the snow patches, which would increase the buoyancy gradient between patch and air above, and thus snowmelt. However, the presence of the IBL diminishes the implications of this downward transport.

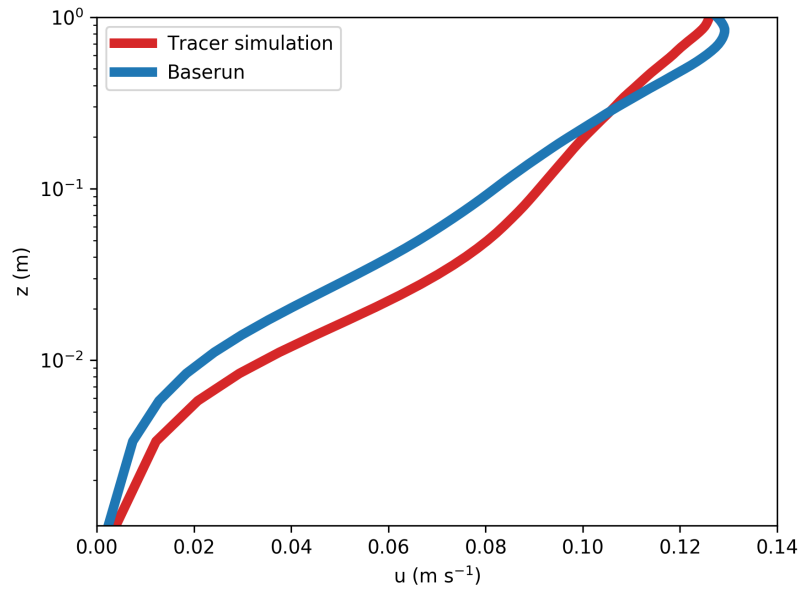


Figure 10 | Wind profile over height. Wind speed in the x-direction (u) against height on a logarithmic axis for the Baserun and the Tracer simulation averaged over the whole horizontal domain from 2000 seconds until 2700 seconds.

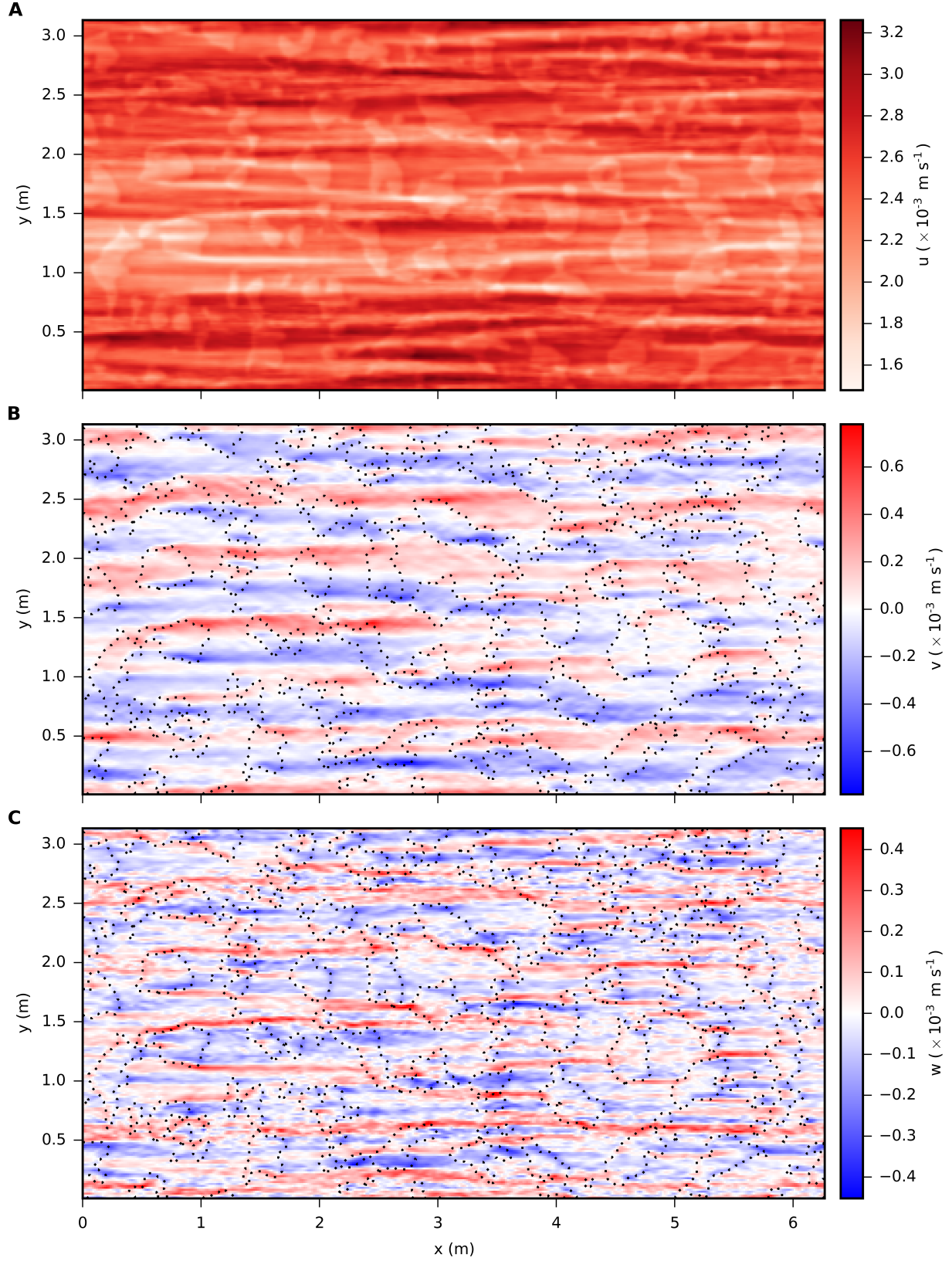


Figure 11 | Wind speeds close to the surface. Wind speed u at $z = 0.001$ m (A), v at $z = 0.001$ m (B) and w at $z = 0.01$ m (C) during the Baserun averaged from 2000 seconds until 2700 seconds. The dotted contours show the location of the implemented snow patches.

3.2 Effects patch size on snowmelt

This section focuses on the implications of changing patch size to the snowmelt to answer the research question. First, the total surface is addressed, whereas subsequently the system is analysed for single snow patches. For snow patches, the analysis is expanded with the development of a simple model.

3.2.1 Total snowmelt

For all the snow patches, clear differences in summed surface buoyancy fluxes arise between all simulations (Figure 12). The highest sensible heat fluxes towards the snow (i.e. most negative) are found in the Tracer simulation, which has no stability effects. This also causes the total surface buoyancy flux for the Tracer simulation to be significantly lower than the other simulations. The stronger surface buoyancy flux also confirms the findings of Section 3.1.1 about the diminishing effect of the IBL on the surface buoyancy fluxes. Furthermore, increasing snow patch size reduces the heat fluxes into the snow patches (Figure 12). The heat fluxes of the Patch 2× simulations decrease with approximately 15% relative to the Baserun. For the Patch 4× simulation, the heat fluxes reduce with approximately 25%. Section 3.2.2 elaborates upon the difference in behaviour.

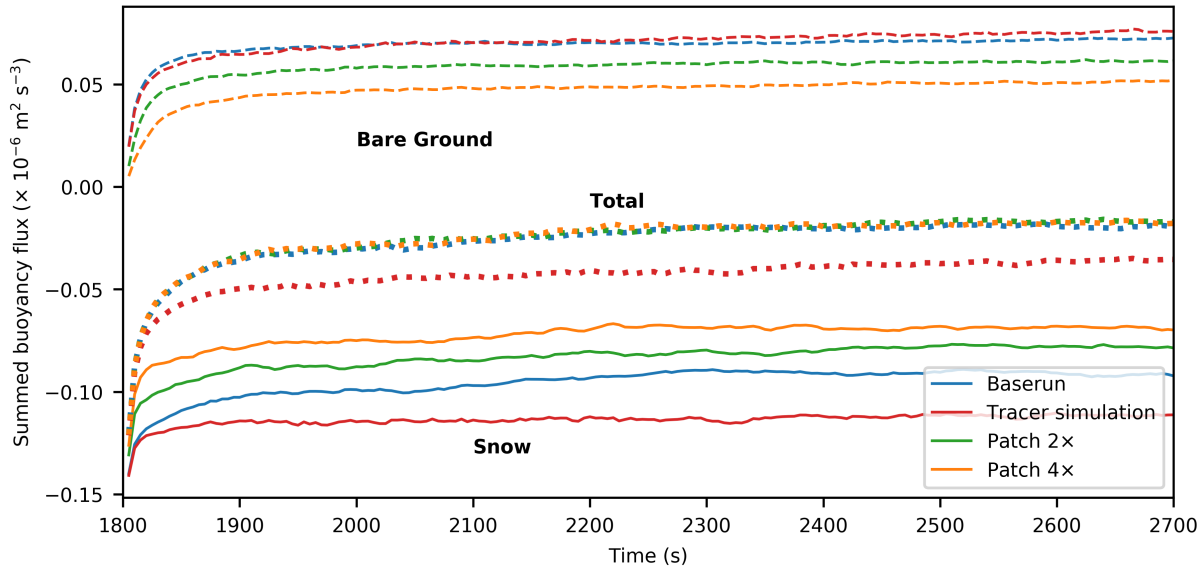


Figure 12 | Summed surface buoyancy fluxes. A time series of the summed surface buoyancy fluxes for the bare ground (dashed), snow (solid) and total surface (dotted).

The total heat fluxes for the Baserun, Patch 2× and Patch 4× coincide approximately, as the differences arising at the snow surface are compensated for at the bare ground surface. So, although the total fluxes are equal, the snowmelt does vary with snow patch size. The Tracer simulation has a significantly reduced total heat flux compared to the Baserun. This is caused by the summed buoyancy fluxes for the bare ground being similar for the Tracer simulation and the Baserun, whereas this is not the case for the snow patches. This

suggests that stability does have little effect on the fluxes above the bare ground, whereas above the snow the surface heat fluxes are clearly affected by stability.

Moreover, the largest adjustment of the buoyancy fluxes after initiation of the simulations is done after less than 100 seconds. However, on a longer term a minor trend is still present for each simulation. For this study, we assume that after the largest adjustment the dominant processes are well developed and suffice to understand the system. We expect that eventually the total summed surface buoyancy fluxes will go to zero. However, as the volume of the channel is relatively large compared to the heat fluxes, it takes relatively long before the whole system has cooled to reach an equilibrium.

3.2.2 Surface fluxes for individual patches

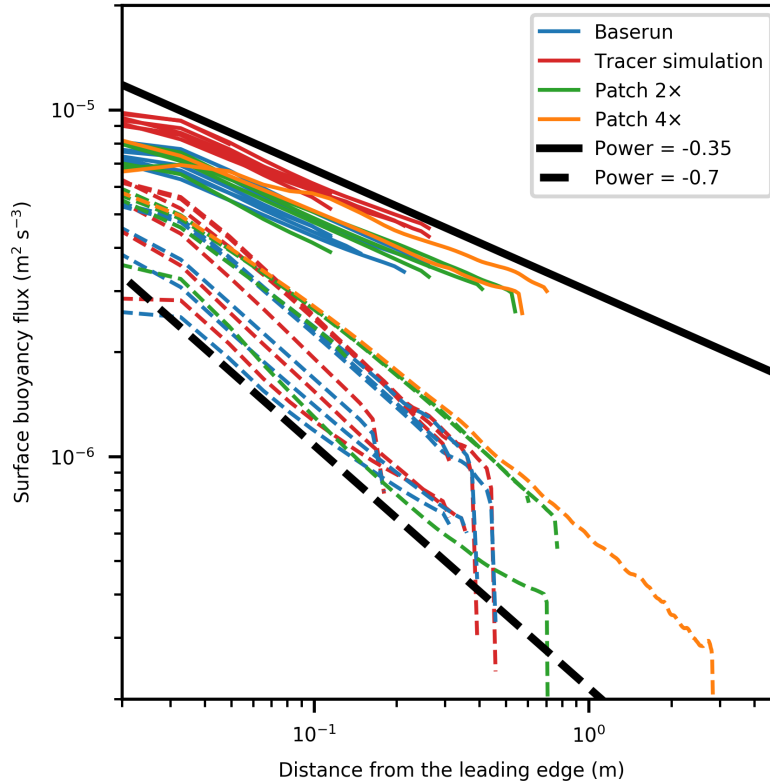


Figure 13 | Surface buoyancy fluxes over single patches of snow (solid) and bare ground (dashed). The surface buoyancy fluxes for individual patches with snow or bare ground as a function of distance from the leading edge on a log-log scale at $y = 1.1$ m. The black lines are implemented trendlines to show the approximate power law decay of the fluxes over distance. The surface fluxes of the snow are multiplied with -1, such that these values can also be plotted on logarithmic axes.

The surface fluxes show for all individual snow and bare ground patches a similar behaviour for each simulation over distance from the leading edge, but differences above snow patches as well as bare ground occur due to varying fluxes at the leading edge (Figure 13). The linear behaviour of the surface fluxes as a function of the

leading edge on logarithmic axes implies that the fluxes decay over distance from the leading edge according to a power law. The power laws take on the following approximate forms:

$$B_{sn}(x) \equiv C_{sn}x^{-0.35}, \quad (22)$$

$$B_{bg}(x) \equiv C_{bg}x^{-0.70}, \quad (23)$$

in which B ($\text{m}^2 \text{s}^{-3}$) is the buoyancy flux, x (m) is the distance from the leading edge and C ($\text{m}^{2.35} \text{s}^{-3}$ for snow and $\text{m}^{2.70} \text{s}^{-3}$ for bare ground) is a constant representing the initial conditions at the leading edge of each patch.

Furthermore, Figure 13 shows that the length of snow patches is the main cause of less snowmelt for larger patches, which was also found by Marsh et al. (1999). The power laws are approximately the same for each patch and simulation, whereas C_{sn} is the same for each simulation except the Tracer simulation. This behaviour explains why larger snow patches reduce the summed surface fluxes into the snow patches and why the Tracer simulation, having no stability effects, has more heat transport towards the snow patches.

Striking is the behaviour of the Tracer simulation, as the decay of the fluxes for this simulation are similar to the decay of the fluxes for the other simulations for snow as well as bare ground, suggesting that stability has little influence on the decay of the surface heat fluxes. However, the Tracer simulation has a relatively lower (higher absolute flux in Figure 13) initial surface flux above the snow, suggesting an influence of the stability on the leading edge conditions.

As mentioned, the system shows also similar behaviour for each bare ground patch during all the simulations. The spread of the buoyancy fluxes is larger than for snow, whereas the Tracer simulation is less outstanding. However, the Tracer simulation is still slightly higher than the Baserun.

Some of the surface fluxes show very high gradients at the downwind edge of the patch (Figure 13). These gradients are caused by the change in sign surface buoyancy flux from bare ground to snow and vice versa, as the bare ground is warmer than the dominant air buoyancy and the snow is colder than the dominant air.

3.2.3 Model development

The decay of the surface heat fluxes are a consequence of the IBL characteristics, especially the formation of the IBLs. To identify the relationship between the surface heat fluxes over snow patches and the IBL characteristics, possible assumptions are studied first and subsequently linked back to the surface heat fluxes with a simple model.

Firstly, as the shape of the vertical profile remains constant while the flow proceeds over the snow patch (Figure 14), the average buoyancy within the IBL remains constant and does not depend on the height of this IBL. For the snow patches the average buoyancy can be defined as a constant fraction (c) of the buoyancy difference between the top and bottom buoyancy, according to

$$c = \frac{\langle b \rangle}{b_{bot} - b_{top}}, \quad (24)$$

in which $\langle b \rangle$ (m s^{-2}) is the averaged buoyancy within the IBL and $b_{bot} - b_{top}$ (m s^{-2}) the difference between the surface and top buoyancy of the IBL. For the snow patch considered in Figure 14, Equation 24 gives $c = 0.41$. As b_{bot} is prescribed when initialising the model and b_{top} is the same as the buoyancy above the IBL, which is constant throughout the whole domain, both variables can be taken as constant during the IBL development.

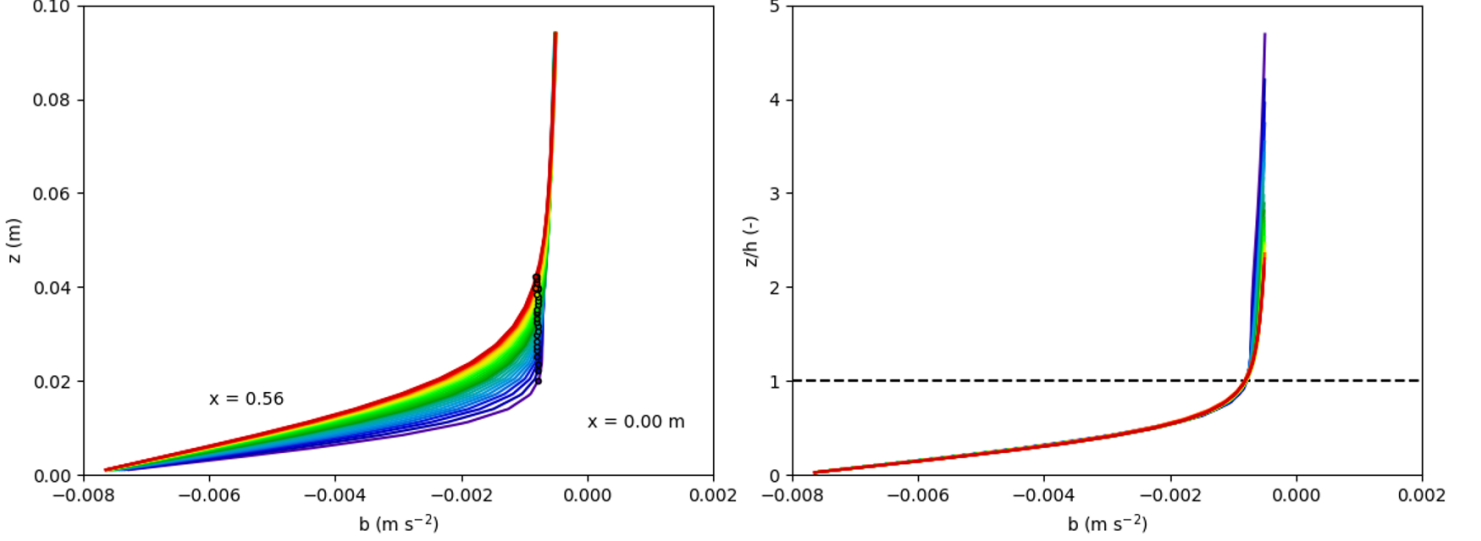


Figure 14 | Vertical profiles of the buoyancy acceleration (b) along the snow patch at $y = 0.83$ m and $x = 1.5$ m in the patch $2\times$ simulation with the IBL height as marker (left) and normalised with the IBL height (right). The height is computed according to the first value seen from the bottom of the gradient of the buoyancy over height below 0.0001 s^{-2} . The first 4 upwind grid cells and 2 downwind grid cells have been removed, as these are located in the transitions region from bare ground to snow and vice versa. The labels with 'x =' show the location of vertical profile related to the downwind distance of the leading edge, whereas the line colors are based on the distance from the leading edge and go from purple to red.

The constant buoyancy within the IBL found for a single patch in Figure 14 is present in all simulations (Figure 15). After a few grid cells from the leading edge, being the transition region, the average buoyancy within the IBL remains constant over distance from the leading edge. Therefore, when developing the simple model, constant average buoyancy is assumed over distance from the leading edge.

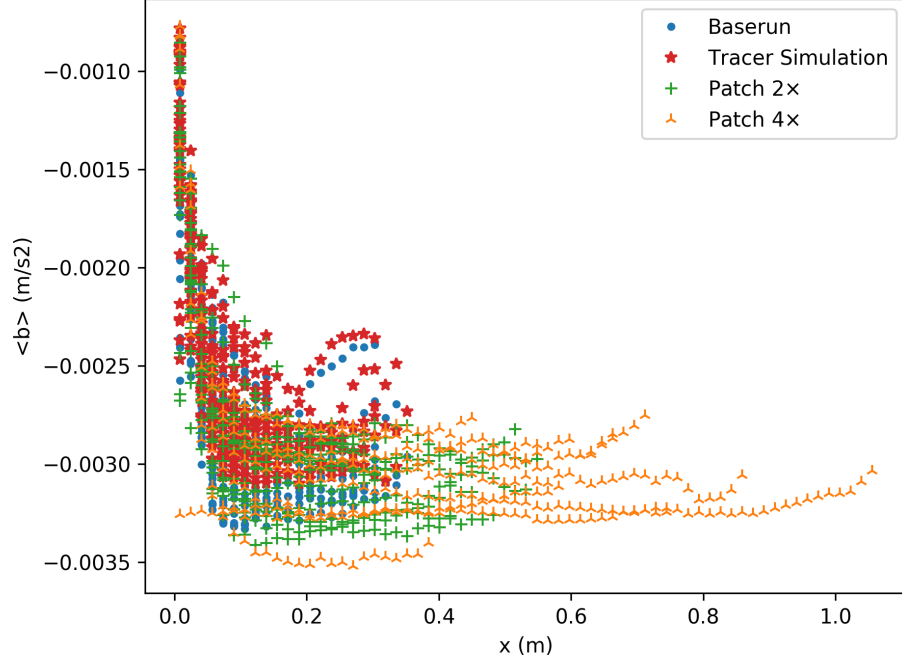


Figure 15 | Scatterplot of the average buoyancy within the IBL ($\langle b \rangle$) versus the downwind distance from the leading edge (x) for all simulations. In total 911 markers are present in the scatterplot, which include the grid cells in the transition regions from bare ground to snow and vice versa.

Secondly, the height of the IBL does not increase linearly with distance from the leading edge (Figure 16). The relationship between both variables seems to follow a power law with the power being less than one, causing the curvature in the scatter plot. However, also some outliers are present, as some clouds of computed heights of the IBL are not near the surface at the leading edge. These outliers show relatively high IBLs, which would be expected further downstream of the leading edge. This is caused by the method to determine the height of the IBL, which solely takes the vertical profiles at each grid point along the cross-section into account. And therefore, the high IBLs at the leading edge can be a consequence of two subsequent patches with little bare ground in between them, causing the IBL to persist at the second patch (e.g. the snow patch in the Baserun around $x = 2.0$ m and $y = 0.8$ m, see Figure 2). Another possible cause is snow patches of which a part, that is not crossed by the cross-section, partially extends further upwind and are relatively close in the y -direction to the crossed leading edge. In such a case, a piece of the snow patch is almost parallel with and close to the made cross-section causing the IBL to build up before the snow patch is recognized in the cross-section (e.g. the snow patch in the patch 2 \times simulation around $x = 2.8$ m and $y = 0.0$ m, see Figure 3). Overall, this shows that the height of the IBL can be described similarly for each simulation with the same power law.

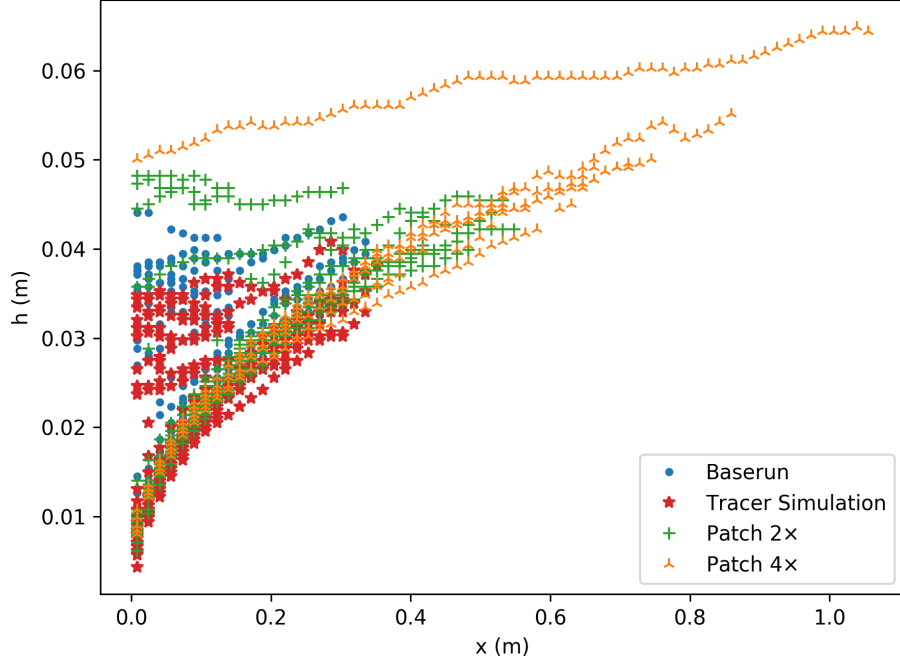


Figure 16 | Scatterplot of the height of the IBL (h) versus the downwind distance from the leading edge (x) for all simulations. The graph is based on the same data as in Figure 15. IBL height is computed the same as done in Figure 14.

Based on the findings of the previous paragraphs a model is developed to describe the IBL development and decay of the heat fluxes as a function of distance from the leading edge. As starting point, the conservation equation of heat is chosen. For the derivation, the Lagrangian perspective is considered, while we have assumed the horizontal turbulent flux gradients are negligible. The turbulent gradients in the x -direction are negligible compared to the advection term, as we assume the latter to be dominant. For the gradients in the y -direction we assume that the conditions at edges of the snow patches do not affect the IBL and the surface flux. These assumptions result in

$$\frac{db}{dt} = -\frac{\partial \overline{w'b'}}{\partial z}, \quad (25)$$

with $\overline{w'b'}$ ($\text{m}^2 \text{s}^{-3}$) being the sensible heat flux. When integrating the right-hand side over height, it follows

$$\begin{aligned} -\int_{z_{bot}}^{z_{top}} \frac{\partial \overline{w'b'}}{\partial z} \delta z &= -(\overline{w'b'}_{top} - \overline{w'b'}_{bot}), \\ &= B_{bot} - \underbrace{B_{top}}_{=0}, \end{aligned} \quad (26)$$

in which B_{top} and B_{bot} are respectively the turbulent buoyancy fluxes at the top and surface of the IBL. B_{top} is assumed to be zero as the buoyancy at the top of the defined IBL is approximately the same as the buoyancy in the mixed layer.

When integrating the left-hand side over height, the Leibniz rule is applied according to

$$\begin{aligned}
\int_{z_{bot}}^{z_{top}} \frac{db}{dt} dz &= \frac{d}{dt} \int_{z_{bot}}^{z_{top}} b dz + \underbrace{b_{bot} \frac{dz_{bot}}{dt}}_{=0} - b_{top} \frac{dz_{top}}{dt}, \\
&= \frac{d}{dt} (\langle b \rangle h) - b_{top} \frac{dh}{dt}, \\
&= \langle b \rangle \frac{dh}{dt} + h \underbrace{\frac{d\langle b \rangle}{dt}}_{=0} - b_{top} \frac{dh}{dt},
\end{aligned} \tag{27}$$

in which $\langle b \rangle$ is the average buoyancy within the IBL, being derived from $\langle b \rangle = \frac{1}{h} \int_{z_{bot}}^{z_{top}} b dz$, b_{top} the buoyancy at the top of the IBL and h (m) the height of the IBL. As z_{bot} is always at the surface, it does not change over time and can therefore be assumed to be constant. Also, we assume $\frac{d\langle b \rangle}{dt}$ to be constant following from Figures 14 & 15. So, the starting equation (25) can be simplified to

$$(\langle b \rangle - b_{top}) \frac{dh}{dt} = B_{bot}. \tag{28}$$

To define the modelled B_{bot} , the definition of van Heerwaarden and Mellado (2016) for free convection is used as starting point

$$B_{bot} = c_1 \kappa^{1/3} (b_{bot} - \langle b \rangle)^{4/3}, \tag{29}$$

with c_1 (-) being a constant with value 0.15 for the case modelled by van Heerwaarden and Mellado (2016) and κ ($\text{m}^2 \text{s}^{-1}$) being thermal diffusivity.

However, this equation is not applicable to our situation, since our system is wind-driven. The equation does not coincide with the observations, as B_{bot} does change with height of the IBL h and not with $\langle b \rangle$, which is constant throughout a single patch (Figures 15 & 16). Therefore, h is included in Equation 29, by analysing the dimensions of the included variables

$$\begin{aligned}
\underbrace{B_{bot}}_{[\text{m}^2 \text{s}^{-3}]} &= \underbrace{c_1}_{[-]} \underbrace{\kappa^{a_1}}_{[\text{m}^{2a_1} \text{s}^{-a_1}]} \underbrace{(b_{bot} - \langle b \rangle)^{a_2}}_{[\text{m}^{a_2} \text{s}^{-2a_2}]} \underbrace{h^{a_3}}_{[\text{m}^{a_3}]}.
\end{aligned} \tag{30}$$

The dimensions of this equation can only be made correct by taking $a_1 = 1$, $a_2 = 1$ and $a_3 = -1$. Thus, resulting in

$$B_{bot} = \frac{c_1 \kappa (b_{bot} - \langle b \rangle)}{h}. \tag{31}$$

So, Equation 28 becomes

$$(\langle b \rangle - b_{top}) \frac{dh}{dt} = \frac{c_1 \kappa (b_{bot} - \langle b \rangle)}{h}. \tag{32}$$

When implementing Equation 24 (i.e. $c = \frac{\langle b \rangle}{b_{bot} - b_{top}}$) in Equation 32, this results in

$$(c_2 b_{bot} - (c_2 + 1) b_{top}) \frac{dh}{dt} = \frac{c_1 \kappa ((1 - c_2) b_{bot} + c_2 b_{top})}{h}, \quad (33)$$

in which c_2 is the constant originating from Equation 24.

Subsequently, this equation still needs to be transformed to x instead of t , to be able to compare the equations with the temporally averaged MicroHH output. This is done according to $\langle u \rangle \frac{\partial}{\partial x} = \frac{d}{dt}$ and results in

$$\langle u \rangle h \frac{dh}{dx} = \alpha, \quad (34)$$

in which $\alpha = \frac{c_1 \kappa ((1 - c_2) b_{bot} + c_2 b_{top})}{(c_2 b_{bot} - (c_2 + 1) b_{top})}$ ($\text{m}^2 \text{s}^{-1}$) and $\langle u \rangle$ (m s^{-1}) being the wind speed averaged over height within the IBL, which is derived from $\langle u \rangle = \frac{1}{h} \int_{z_{bot}}^{z_{top}} u dz$.

To elaborate Equation 34, the relation between $\langle u \rangle$ and h must be implemented. However, as most IBLs are within the viscous sublayer and buffer layer (Figure 10), no simple equations suffice to describe the behaviour of $\langle u \rangle$ in the IBL. The actual relation depends on the the viscous sublayer wind profile, being linear, as well as the log profile. For now, the relation between h and $\langle u \rangle$ is taken from the model output (Figure 17), which resembles slightly less than a proportional relation. When fitting a simple power law, $\langle u \rangle = c_3 h^\beta$, this results in β being in the order of 0.8 - 0.9. The constant c_3 ($\text{m}^{1-\beta} \text{s}^{-1}$) value differs for the Tracer simulation compared to the other simulations (Figure 17), as was found also in Section 3.1.2, about the wind components.

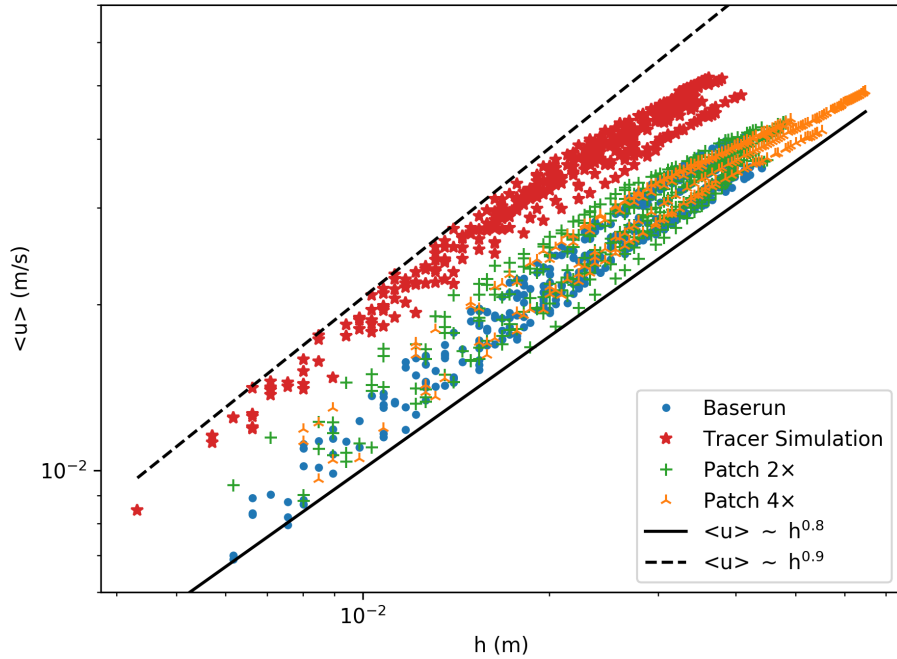


Figure 17 | Scatterplot of the average wind speed within the IBL ($\langle u \rangle$) versus the height of the IBL (h) for all simulations. The graph is based on the same data as in Figure 16.

Subsequently, after implementing the relation between $\langle u \rangle$ and h , the decay of the surface fluxes over the leading edge is calculated by integrating and transforming Equation 34 to an equation for h

$$\int c_3 h^{\beta+1} dh = \alpha \int dx, \quad (35)$$

$$\frac{c_3}{\beta+2} h^{\beta+2} = \alpha x, \quad (36)$$

$$h = \left(\frac{\alpha(\beta+2)}{c_3} x \right)^{\frac{1}{\beta+2}}. \quad (37)$$

When substituting Equation 37 for h into Equation 30, which described the surface buoyancy flux as a function of height of the IBL, this results in

$$B_{bot} = \gamma x^{-\frac{1}{\beta+2}}, \quad (38)$$

with $\gamma = c_1 \kappa ((1 - c_2) b_{bot} + c_2 b_{top}) \left(\frac{(\frac{c_1 \kappa ((1 - c_2) b_{bot} + c_2 b_{top})}{(c_2 b_{bot} - (c_2 + 1) b_{top})})(\beta + 2)}{c_3} \right)^{-\frac{1}{\beta+2}}$ as a constant.

Thus, when assuming $\beta = 0.85$,

$$B_{bot} \sim x^{-0.35},$$

which coincides with the found decay of the surface buoyancy flux over the distance from the leading edge for the snow patches (Figure 13).

The final equation also illustrates how the Tracer simulation and the Baserun relate to each other. The decay of the two simulations is similar, which also returns in the final equation, as the power in the power law is the same for both simulations, namely $-\frac{1}{\beta+2}$. The constant c_3 , however, introduced in the relation between $\langle u \rangle$ and h , is higher for the Tracer simulation (Figure 16). The higher c_3 affects the magnitude of the surface buoyancy fluxes as a multiplication factor, such that the surface buoyancy fluxes in the Tracer simulation enhance compared to the Baserun. It follows that the value of c_3 depends on stability in this simple model.

3.3 Rescaling to atmospheric values

The previously presented results suggest that wind shear predominantly affects the surface buoyancy fluxes over single patches of snow and bare ground (e.g. Figures 13). Also, when calculating the Richardson number (i.e. $-\frac{b_{sn}\delta}{u^2}$) based on the buoyancy (Figure 6) and wind profiles (Figures 10 and 17), the influence of wind shear emerges. The difference between b_{sn} and b_{ml} becomes -0.007 m s^{-2} instead of -0.008 m s^{-2} , since b_{ml} is not 0 m s^{-2} , but approximately -0.001 m s^{-2} . The height of the studied layer, i.e. the IBL, is on average approximately 0.03 m , whereas the wind speed at the top of the IBL is 0.05 m s^{-1} . Thus,

$$Ri_{sn} = -\frac{-0.007 \times 0.03}{0.05^2} = 0.084, \quad (39)$$

suggesting that the studied flow region is near-neutral and dominated by wind-shear.

Therefore, the surface buoyancy and time scaling is done via (see section 2.2.3 for explanation)

$$\begin{aligned} B_{sn} &= ub_{sn}, \\ t_{adv} &= \frac{\delta}{u}. \end{aligned} \quad (40)$$

Thus, the surface buoyancy fluxes and time are respectively divided by 4.9×10^{-4} and 0.58. The length scales are multiplied with 100 to arrive at realistic distance values. This is obtained from the ratio

$$\frac{\delta_{real}}{\delta_{sim}} = \frac{100\text{m}}{1\text{m}} = 100. \quad (41)$$

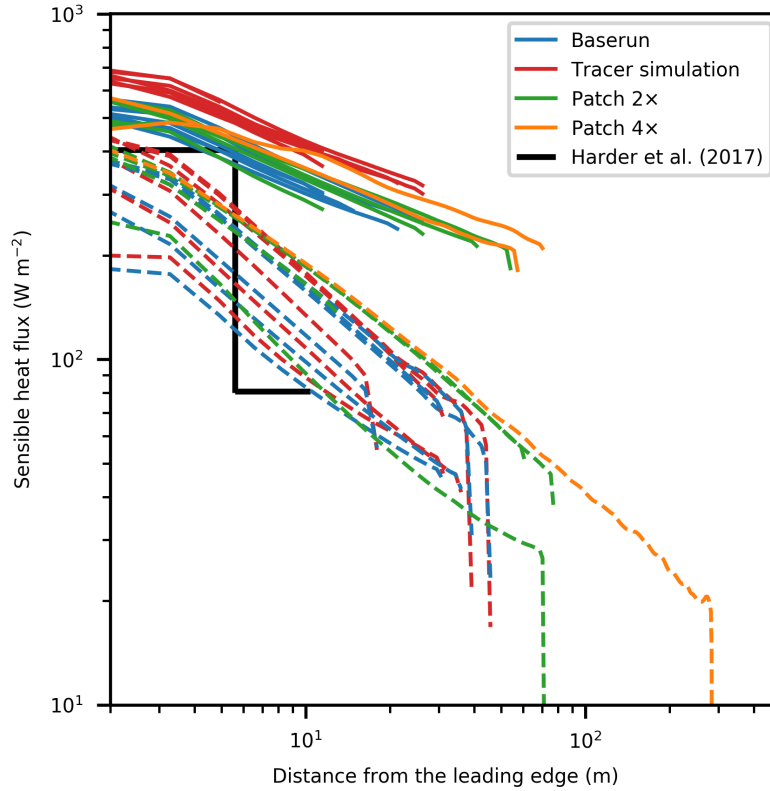


Figure 18 | Rescaled sensible heat flux over single patches of snow (solid) and bare ground (dashed). The sensible heat fluxes for individual patches with snow or bare ground as a function of distance from the leading edge on a log-log scale at $y = 1.1$ m. The surface fluxes of the snow are multiplied with -1, such that these values can also be plotted on logarithmic axes.

The measurements done by Harder et al. (2017) show values slightly above 400 W m^{-2} for the first 3.6 m (Figure 18). The rescaled sensible heat fluxes are approximately 500 W m^{-2} at the leading edge and reduce to approximately 450 W m^{-2} during the first 3.6 m. For the following 4.8 m, Harder et al. (2017) reported a reduction in sensible heat flux to approximately 20% of values found for the first 3.6 m. In the Baserun,

which has a similar dominant snow patch pattern as Harder et al. (2017), this reduction is not found. The sensible heat flux above the snow does never reduce to these fractions, but only halves compared to the maximum values for the surface sensible heat flux.

For bare ground, the sensible heat fluxes are on average slightly less than 1.5 to 2 times lower at the leading edge compared to the snow patches (respectively $\sim 300 \text{ W m}^{-2}$ versus $\sim 500 \text{ W m}^{-2}$). However, the spread for the sensible heat fluxes above bare ground is larger than for snow, as this varies from less than 200 W m^{-2} to more than 400 W m^{-2} at the leading edge.

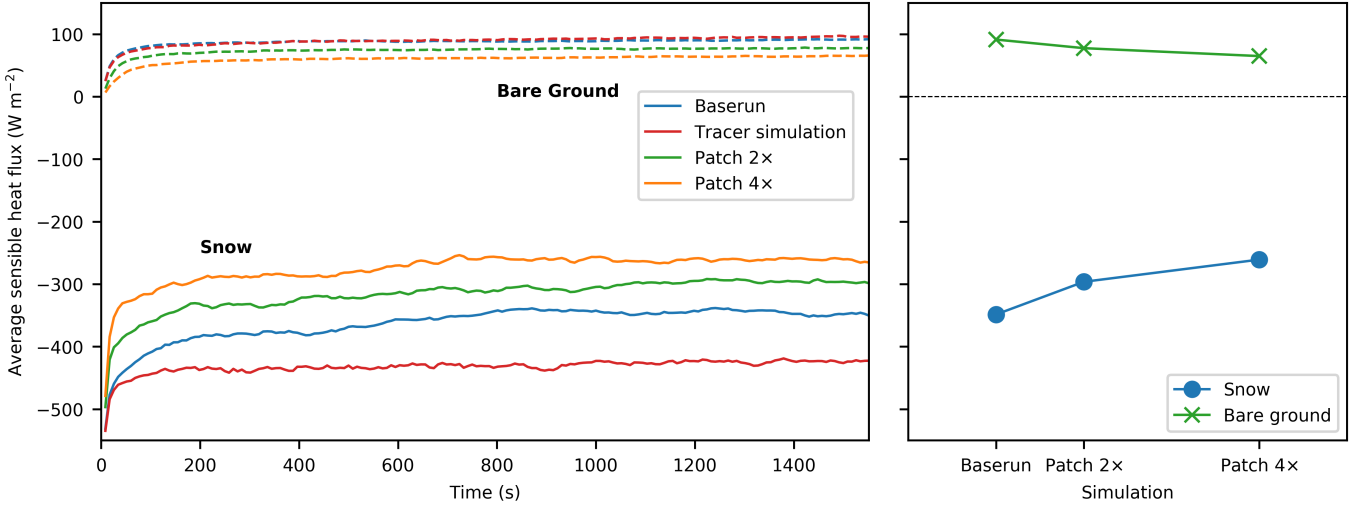


Figure 19 | Rescaled average surface buoyancy fluxes. A Rescaled time series of the average surface buoyancy fluxes for the snow and bare ground (left) and final average sensible heat fluxes from the Baserun, Patch 2 \times and Patch 4 \times for snow and bare ground (right).

The rescaled average sensible heat fluxes above the snow patches are -349 W m^{-2} , -296 W m^{-2} and -261 W m^{-2} for respectively the Baserun, Patch 2 \times , Patch 4 \times (Figure 19). For the bare ground, the average sensible heat fluxes are respectively 91 W m^{-2} , 78 W m^{-2} and 65 W m^{-2} . The reductions of the sensible heat fluxes imply that for larger patches the snowmelt due to local-scale advection is lower, however the reductions in melt are not proportionally related to the increase in patch and element size (Figure 19), which was also found by Marsh et al. (1999).

After initiating the simulations, the largest changes occur for each simulation within 200 real seconds. When transforming this time to distance by making use of the measured averaged wind speed, being 6.4 m s^{-1} , this comes down to $200 \text{ s} \times 6.4 \text{ m s}^{-1} = 1280 \text{ m}$. So, for this simulated flow with patchy snow cover, it takes approximately 1.3 km before it is in steady state.

4 Discussion

The main goal of this study is to identify the relationship between snow patch size and surface heat fluxes, which helps understanding snowmelt due to local-scale advection for a patchy snow cover. During this discussion, we critically review the results of this study. Also, identified limitations and recommendations will be brought up.

This study aimed to provide insight in the role of snow patch size during snowmelt of patchy snow cover. The results of this study show a non proportional relation between the increase in patch size and snowmelt, since a doubling and quadrupling of snow patch size cause the snowmelt for an infinitely large domain with a 25% snow cover to reduce with respectively 15% and 25%. Moreover, this influence is solely caused by the length of the snow patches, because the sensible heat fluxes are the same order of magnitude at the leading edge of a snow patch and decay similarly, whereas the larger patches extend further and have lower sensible heat fluxes at the downwind edge, reducing the average sensible heat fluxes.

It should be brought up that for the Patch 4 \times , which had a 25% reduction in snowmelt, the nondimensional number $\frac{\delta}{\lambda_{elem}}$ was rather low and could have affected the outcome. During this simulation the number was 0.83, whereas the number was originally designed to be approximately 1 or higher, such that the relative snow patch size would not be too large. The implications could be that the largest turbulent structures arising, due to the snow patches, did not have enough space to develop and are therefore affected by the horizontal domain of the simulation. However, other results show no clear deviations from the expectation, and thus we assume that the influence of this value of the nondimensional number is relatively minor to non-existent.

The results of this study shows the potential of DNS, compared to other simulation types, such as LES. Whereas studies making use of LES, such as Schlögl et al. (2018), report large errors compared with measurements. For this research, the flow characteristics are similar to controlled and field measurements. Next to the measurements done by Harder et al. (2017) in the field, the measurements of Mott et al. (2016) in a wind tunnel also show similar shapes for the buoyancy profiles above snow patches. Also, the vertical profiles of the buoyancy above the bare ground show similar profiles compared to the measurements of Harder et al. (2017), when extrapolating the development of the simulated profiles to further distances from the leading edge of the bare ground patch. The height of the IBLs clearly differs, but this outcome seems promising for future research. Especially, because the findings done on the characteristics of the IBL, such as a constant $\langle b \rangle$ over distance from the leading edge, can probably be considered by others.

This study did not look further into the behaviour of the flow over bare ground as it was not relevant for answering the research question. However, similar to above snow, the sensible heat fluxes show the same behaviour for each simulation, although the spread of the found values was larger. It is also unclear, which processes dissipate the cold air plume dominating the vertical temperature profiles, which takes much longer than the warm air plume above the snow. We therefore recommend for future studies to look further into the behaviour of the flow above the bare ground as local-scale advection of sensible (and latent) heat depends not only on the fluxes towards the snow, but also on the source of heat, being the bare ground. Therefore, more research into this will complement the understanding of local-scale advection.

Possibly, the mismatch in the decay of the surface buoyancy fluxes is caused by the relatively low Re_τ applied for the simulations (i.e. $\sim 6 \times 10^6$ vs 590). This was done based on the results of Moser et al. (1999), who

showed large differences between $Re_\tau = 180$ and $Re_\tau = 395$, whereas $Re_\tau = 590$ has similar bulk quantities and variances as the latter simulation. As a consequence of the low Re_τ , the viscous sublayers are relatively high, being approximately 1 m, although this layer is approximately 2 orders of magnitude smaller in reality. This has as advantage that the high viscous sublayers also contain enough grid points to resolve the flow towards the surface and causes relatively cheap simulations (Ferziger and Peric, 2002). However as mentioned, the low Re_τ could have also caused the mismatches in behaviour between the simulations, as adjusting the Re_τ also possibly has affected the surface momentum fluxes, of which $\frac{U}{u_\tau}$ is a measure, and thus also the heat fluxes. This follows from a general law for wall flows for mean velocity profiles

$$\frac{U}{u_\tau} = F\left(\frac{z}{\delta}, Re_\tau\right), \quad (42)$$

in which U is the wind speed (m s^{-1}), u_τ the friction velocity (m s^{-1}), F a yet unknown nondimensional function depending on the flow characteristics, z the height (m) and δ is the typical height scale (Pope, 2000). The nondimensional function could also be altered by the substantial height of the viscous sublayer in our simulations, as the flow characteristics that determine the function are different for the viscous sublayer compared to the log-layer.

Furthermore, the low Re has caused the fluxes in the IBL to be predominantly diffusive, whereas in reality the turbulent fluxes are more likely to dominate. This diffusive dominance probably has caused the mismatch in height of the IBL, since the height of a diffusive layers scales with $Re^{-3/4}$. Moreover, it might have contributed to the mismatch in decay of the sensible heat fluxes compared with Harder et al. (2017). As the typical diffusive timescales are larger than the typical turbulent timescales, the typical time- and length-scales of the processes in the IBL are relatively large compared to reality. One of these processes affected by this, could be the decay of the sensible heat fluxes over distance from the leading edge of a snow patch.

To uncover whether the surface fluxes are dependent of the Re_τ , we recommend to do simulations with higher Re_τ as the simulations can be compared with each other by normalising due to comparing by making use of the Re_τ . In case it turns out that the surface fluxes are independent of the Re_τ , it can be inferred that the system at hand is self-similar. Also, this will allow the simulations to be relatively cheap, as the Re^3 is proportional to the computational costs of simulations (Tennekes and Lumley, 1972), and still suffice to describe the system.

When enhancing Re , the scale of the smallest eddies, i.e. the Kolmogorov length scale η , also reduces as previous studies have shown (Pope, 2000)

$$\frac{\eta}{\delta} \sim Re^{-3/4}, \quad (43)$$

in which δ is the length scale for the largest eddies. Therefore, this will require an enhancement of the resolution compared to this study. As advantage this study has, that the experiments have been halved compared to Moser et al. (1999), to save computational costs. Similar to other studies, we have assumed that the highest energy containing wavenumber is that much larger than the Kolmogorov length for the simulations, i.e. the resolution, such that this will not affect the outcome of the simulations. However, for the Baserun, we assume that the largest turbulent structures have a typical length scale similar to the typical

length scale for snow patches (0.15 m), which is less 10 times larger than the resolution $\Delta x = \frac{2\pi}{384}$. So, when enhancing Re , it is recommended to increase the resolution, possibly to the original resolution.

Another option for the mismatch could be due to an inaccuracy during the nondimensional scaling of the wind speed and temperature difference between the snow and atmosphere. As Harder et al. (2017) reported a wind speed of 6.4 m s^{-1} , this value is also considered in our dimensional analysis and related 0.11 m s^{-1} , which was the average wind speed over the whole channel in the case of Moser et al. (1999). However, the reported wind speed was measured at 1.8 meter above the ground, thus implying that the average wind speed for the whole air column under consideration would be higher. Consequently, wind shear increases, and thus also the fluxes towards the surface. Also, the temperature difference between the snow and atmosphere has been possibly overestimated, causing the sensible heat flux to increase. The graphs presented by Harder et al. (2017) show the temperatures of bare ground and atmosphere to be constant near the surface, being $6.4 \text{ }^{\circ}\text{C}$. However, for the dimensional analysis, the atmospheric temperature mentioned by Harder et al. (2017), i.e. $7.9 \text{ }^{\circ}\text{C}$, has been used.

In the studied system, the influence of stability seems to be negligible for the relative decay of the surface fluxes over distance from the leading edge, since the surface heat fluxes in the Tracer simulation show the same decay as the Baserun. However, the snowmelt in the Tracer simulation is still higher as the absolute sensible heat fluxes at the leading edge are higher for the Tracer simulation than the Baserun. We expect, that the decay is similar due to the relative high wind speeds and low temperature difference between the snow and bare ground; 6.4 m s^{-1} and 8 K respectively. Overall, this causes the shear induced turbulence to dominate over the buoyancy induced wind speed. Possibly, the higher wind speeds near the surface for the Tracer simulation have also caused the higher absolute sensible heat fluxes for this simulation compared to the Baserun. Therefore, it would be interesting to reduce the wind speed and increase the temperature difference between the snow and bare ground, to identify which Ri_{sn} is needed for stability to become a more important factor on the surface heat fluxes, as multiple studies suggest the role of stability on snowmelt (e.g. Dadić et al., 2013; Essery et al., 2006).

The characteristic of dominance of shear induced turbulence was also used for the development of a simple model that described the surface fluxes, as no stability corrections were considered during the derivation. The final step of the derivation showed that the average wind speed $\langle u \rangle$ within the IBL, was crucial to end up at the eventual relation found between the surface buoyancy fluxes and the distance from the leading edge. The decay of the surface buoyancy fluxes increases with an increase in the gradient $\frac{d\langle u \rangle}{dh}$, and as such also depends on the average wind speed over the whole column. This relationship also causes the absolute values of the surface buoyancy fluxes in the Tracer simulation to be higher than the Baserun, as the Tracer simulation has an enhanced average wind speed within the IBL, due to the found influence of buoyancy to the wind components in the Baserun. Overall, increasing the wind speed, as suggested before, would also affect the decay of the surface heat fluxes in the developed model. However, the difference between the Tracer simulation and Baserun would remain present, due to the introduced constant, which is influenced by stability, originating from the relation between $\langle u \rangle$ and h .

5 Conclusion

The aim of this study was to identify the role of patch size on local-scale advection of sensible heat towards a patchy snow cover by using direct numerical simulations in MicroHH. The designed numerical experiments with a 25% patchy snow cover were based on measurements done by Harder et al. (2017) on a 15 m single snow patch on a flat surface.

We found that when doubling and quadrupling the snow patch size of Harder et al. (2017), the snowmelt reduces with respectively 15% and 25%. As the sensible heat fluxes above the snow patches in each simulation behave approximately the same, the main cause of the reduction in sensible heat fluxes was caused by the longer patches itself. The simulations revealed that at the leading edge of a snow patch the sensible heat fluxes were of a similar order of magnitude, whereas the decay over distance was also similar and, thus, independently of patch size. However, as longer snow patches extend further, the decay also extends, such that the average sensible heat flux towards longer patches reduces, and as such also reduces average snowmelt. Moreover, the total sensible heat fluxes of the snow combined with the bare ground showed no sign of the changing snow patch size and the accompanied reductions in snowmelt. In essence, the found reductions and unaltered total fluxes show the significance of considering also typical snow patch size when predicting regional snowmelt.

Furthermore, all performed simulations show the ability of MicroHH to simulate the leading edge effect, and also clear IBLs form over snow patches as well as bare ground. The characteristics of these IBLs differ as the one above the snow is highly stable, whereas the one over bare ground clearly shows dissipation of the cold air remnants originating from the cold snow. One of these characteristics was the constant average temperature within the IBL over the course of a snow patch, which can be helpful during, for instance, future measurement campaigns.

The sensible heat fluxes measured by Harder et al. (2017) were lower than the sensible heat fluxes in a comparable simulation. Some potential causes were identified, of which a too high temperature difference between the snow and atmosphere and too low modelled wind speed are the most obvious candidates. Also, the latter cause is a potential cause in the found mismatch in decay of the sensible heat flux, as wind speed is also a measure for wind shear and, thus, also affects the decay of the surface heat fluxes over distance. Another possible cause is the relatively low Reynolds number, which also might have caused a mismatch in the height of the IBLs.

An additional simulation, in which stability did not affect the flow, revealed that in the studied circumstances stability does not have any effect on the behaviour of the flow along the course of a snow patch. This additional simulation without stability effects showed the same decay of the sensible heat fluxes along the course of a snow patch as the simulation with stability effects. We suspect that the the windy circumstances under which the measurements were done, caused the wind shear driven turbulence to dominate over the buoyancy driven turbulence in this case. However, stability effects did have a reducing influence on the overall wind speed and, thus, also wind shear, causing the sensible heat fluxes to be constantly lower for the the simulation in which stability effects were included.

The general behaviour of the height of the IBL and sensible heat flux over distance from the leading edge were also captured within a developed model, consisting of just a few equations. This new model was well

able to describe the simulated behaviour of the height of the IBL and surface buoyancy fluxes over snow as a function of distance from the leading edge. Overall, the new model shows the potential of developing a computationally cheap method for predicting wind-driven snowmelt with large-scale models.

Overall, this study has shown the potential of DNS when simulating a patchy snow cover or more in general a heterogeneous surface, especially compared to the errors that have been found for other simulation types. The study has helped in the understanding one of the main snowmelt processes, being the sensible heat flux and the role of changing patch size within that picture. The magnitude of the found sensible heat fluxes at the leading edge expresses the importance of understanding how the process of local-scale advection of sensible heat works. Furthermore, the sensible heat flux behaviour along the course of a snow patch being independent of patch size can be of great use in continuation studies. However, it is still unclear whether the simulations are influenced by the relatively low Reynolds numbers and also the role of stability in less windy circumstances is yet unclear and would need further research.

References

- Balsamo, G., Beljaars, A., Scipal, K., Viterbo, P., van den Hurk, B., Hirschi, M., and Betts, A. K. (2009). A Revised Hydrology for the ECMWF Model: Verification from Field Site to Terrestrial Water Storage and Impact in the Integrated Forecast System. *Journal of Hydrometeorology*, 10:623–643.
- Barnett, T. P., Adam, J. C., and Lettenmaier, D. P. (2005). Potential impacts of a warming climate on water availability in snow-dominated regions. *Nature*, 438:303–309.
- Berghuijs, W. R., Woods, R. A., and Hrachowitz, M. (2014). A precipitation shift from snow towards rain leads to a decrease in streamflow. *Nature Climate Change*, 4:583–586.
- Coleman, G. N., Ferziger, J. H., and Spalart, P. R. (1990). A numerical study of the turbulent ekman layer. *Journal of Fluid Mechanics*, 213:313–348.
- Dadic, R., Mott, R., Lehning, M., Carenzo, M., Anderson, B., and Mackintosh, A. (2013). Sensitivity of turbulent fluxes to wind speed over snow surfaces in different climatic settings. *Advances in Water Resources*, 55:178–189.
- Deardorff, J. W. (1972). Numerical Investigation of Neutral and Unstable Planetary Boundary Layers. *Journal of the Atmospheric Sciences*, 29:91–115.
- Essery, R., Granger, R., and Pomeroy, J. (2006). Boundary-layer growth and advection of heat over snow and soil patches: Modelling and parameterization. *Hydrological Processes*, 20:953–967.
- Ferziger, J. and Peric, M. (2002). *Computational Methods for Fluid Dynamics*. Springer.
- Fujita, K., Hiyama, K., Iida, H., and Ageta, Y. (2010). Self-regulated fluctuations in the ablation of a snow patch over four decades. *Water Resources Research*, 46:1–9.
- Garratt, J. R. (1990). The internal boundary layer - A review. *Boundary-Layer Meteorology*, 50:171–203.
- Granger, R. J., Essery, R., and Pomeroy, J. W. (2006). Boundary-layer growth over snow and soil patches: Field observations. *Hydrological Processes*, 20:943–951.
- Granger, R. J., Pomeroy, J. W., and Parviainen, J. (2002). Boundary-layer integration approach to advection of sensible heat to a patchy snow cover. *Hydrological Processes*, 16:3559–3569.
- Harder, P., Pomeroy, J. W., and Helgason, W. (2017). Local-Scale Advection of Sensible and Latent Heat During Snowmelt. *Geophysical Research Letters*, 44:9769–9777.
- Kawamura, H., Ohsaka, K., Abe, H., and Yamamoto, K. (1998). Dns of turbulent heat transfer in channel flow with low to medium-high prandtl number fluid. *International Journal of Heat and Fluid Flow*, 19(5):482 – 491.
- Liston, G. E. (1995). Local Advection of Momentum, Heat and Moisture during the Melt of Patch Snow Covers. *Journal of Applied Meteorology*, 34:1705–1716.
- Mankin, J. S., Viviroli, D., Singh, D., Hoekstra, A. Y., and Diffenbaugh, N. S. (2015). The potential for snow to supply human water demand in the present and future sources. *Environmental Research Letters*, 10:1–10.
- Marsh, P., Neumann, N., Essery, R., and Pomeroy, J. (1999). Model estimates of local advection of sensible heat over a patchy snow cover. In *Interactions between the Cryosphere, Climate and Greenhouse Gases*, pages 103–110.
- Moin, P. and Mahesh, K. (1998). Direct numerical simulation: A tool in turbulence research. *Annual Review of Fluid Mechanics*, 30:539–578.

- Monin, A. S. and Obukhov, A. M. (1954). Basic laws of turbulent mixing in the surface layer of the atmosphere. *Trudy geofiz. inst. AN SSSR*, 24:163–187.
- Moser, R. D., Kim, J., and Mansour, N. N. (1999). Direct numerical simulation of turbulent channel flow up to $Re_\tau = 590$. *Physics of fluids*, 11(4):943–945.
- Mott, R., Daniels, M., and Lehning, M. (2015). Atmospheric Flow Development and Associated Changes in Turbulent Sensible Heat Flux over a Patchy Mountain Snow Cover. *Journal of Hydrometeorology*, 16:1315–1340.
- Mott, R., Egli, L., Grünwald, T., Dawes, N., Manes, C., Bavay, M., and Lehning, M. (2011). Micrometeorological processes driving snow ablation in an Alpine catchment. *The Cryosphere*, 5:1083–1098.
- Mott, R., Gromke, C., Grünwald, T., and Lehning, M. (2013). Relative importance of advective heat transport and boundary layer decoupling in the melt dynamics of a patchy snow cover. *Advances in Water Resources*, 55:88–97.
- Mott, R., Paterna, E., Horender, S., Crivelli, P., and Lehning, M. (2016). Wind tunnel experiments: Cold-air pooling and atmospheric decoupling above a melting snow patch. *Cryosphere*, 10:445–458.
- Mott, R., Schlögl, S., Dirks, L., and Lehning, M. (2017). Impact of Extreme Land Surface Heterogeneity on Micrometeorology over Spring Snow Cover. *Journal of Hydrometeorology*, 18:2705–2722.
- Pohl, S., Marsh, P., and Liston, G. E. (2006). Spatial-Temporal Variability in Turbulent Fluxes during Spring Snowmelt. *Arctic, Antarctic and Alpine Research*, 38:136–146.
- Pope, S. (2000). *Turbulent Flows*. Cambridge University Press.
- Schlögl, S., Lehning, M., and Mott, R. (2018). How Are Turbulent Sensible Heat Fluxes and Snow Melt Rates Affected by a Changing Snow Cover Fraction? *Frontiers in Earth Science*, 6.
- Schlögl, S., Lehning, M., Nishimura, K., Huwald, H., Cullen, N. J., and Mott, R. (2017). How do Stability Corrections Perform in the Stable Boundary Layer Over Snow? *Boundary-Layer Meteorology*, 165:161–180.
- Tennekes, H. and Lumley, J. L. (1972). *A first course in turbulence*. MIT press.
- van Heerwaarden, C. C. and Mellado, J. P. (2016). Growth and Decay of a Convective Boundary Layer over a Surface with a Constant Temperature. *Journal of the Atmospheric Sciences*, 73:2165–2177.
- van Heerwaarden, C. C., Mellado, J. P., and De Lozar, A. (2014). Scaling Laws for the Heterogeneously Heated Free Convective Boundary Layer. *Journal of the Atmospheric Sciences*, 71:3975–4000.
- van Heerwaarden, C. C., van Stratum, B. J. H., Heus, T., Gibbs, J., Fedorovich, E., and Mellado, J. P. (2017). MicroHH 1.0: a computational fluid dynamics code for direct numerical simulation and large-eddy simulation of atmospheric boundary layer flows. *Geoscientific Model Development*, 10:3145–3165.
- Viviroli, D., Dürr, H. H., Messerli, B., Meybeck, M., and Weingartner, R. (2007). Mountains of the world, water towers for humanity: Typology, mapping, and global significance. *Water Resources Research*, 43:1–13.
- Weismann, R. N. (1977). Snowmelt: A Two-Dimensional Turbulent Diffusion Model. *Water Resources Research*, 13(2).